January 2023

Predicting Ash Deposition In A Cyclone-Fired Coal Boiler Under Variable Load Conditions

Evan Bloom

Predicting Ash Deposition in a Cyclone-Fired Coal Boiler Under Variable Load Conditions

by

Evan Bloom

Bachelor of Science, University of North Dakota, 2021

A Thesis

Submitted to the Graduate Faculty

of the

University of North Dakota

In partial fulfillment of the requirements

for the degree of Master of Science

Grand Forks, North Dakota

May, 2023

This thesis, submitted by Evan Bloom in partial fulfillment of the requirements for the Degree of Master of Science from the University of North Dakota, has been read by the Faculty Advisory Committee under whom the work has been done and is hereby approved.

Dr. Gautham Krishnamoorthy, Chairperson

Dr. Wayne Seames,

Dr. Steve Benson

This thesis is being submitted by the appointed advisory committee as having met all of the requirements of the School of Graduate Studies at the University of North Dakota and is hereby approved.

Chris Nelson
Dean of the School of Graduate Studies

Date

PERMISSION

Title: Predicting Ash Deposition in a Cyclone-Fired Coal Boiler Under Variable Load Conditions

Department: Chemical Engineering

Degree: Master of Science

In presenting this thesis in partial fulfillment of the requirements for a graduate degree from the University of North Dakota, I agree that the library of this University shall make it freely available for inspection. I further agree that permission for extensive copying for scholarly purposes may be granted by the professor who supervised my thesis work, or in his absence, by the Chairperson of the department or the dean of the School of Graduate Studies. It is understood that any copying or publication or other use of this thesis or part thereof for financial gain shall not be allowed without my written permission. It is also understood that due recognition shall be given to me and the University of North Dakota in any scholarly use which may be made of any material in my thesis.

Evan Bloom

May 2023

Table of Contents

List of Figures

Figure *Page*

List of Tables

Nomenclature

A	Urbain viscosity empirical parameter
A_s	surface area (m^2)
A_2O_3	mole fraction of amphoterics
α	fraction of network modifiers and amphoterics
$b_{0\text{-}11}$	empirical constants for Senior/Srinivasachar viscosity model
a_{1-3}	coefficients for Morsi-Alexander drag law
B	viscosity models empirical parameter
B_x	Urbain viscosity empirical parameters (x ranges from 0 to 3)
C_D	drag coefficient
C_p	specific heat
d, D	diameter (m)
E	energy
E_k	kinetic energy (J)
$\bar{F}$	additional acceleration term
$\vec{F}$	external body force vector
F_D	hydrodynamic drag force (N)
$\bar{g}, \vec{g}$	gravitational force vector (m/s^2)

h	specific enthalpy
h_c	convective heat transfer coefficient
$\vec{J}, \bar{J}$	diffusive flux
J	joules
k	thermal conductivity
k_{eff}	effective thermal conductivity
k_t	turbulent thermal conductivity
m	mass (kg)
MO	mole fraction of network modifiers
p	pressure
PKE	particle kinetic energy
Re	Reynolds number (dimensionless)
S	volumetric source term
S_h	volumetric source term that includes heat of chemical reaction
S_m	volumetric source term to represent mass addition
t	time (s)
T	temperature (K)
T_∞	free stream/surrounding fluid temperature (K)

u, $\bar{u}$	velocity (m/s)
$\vec{v}$	velocity vector
x	molar mass fraction
Y	local mass fraction

Greek Symbols

ε	emissivity
θ_R	radiation temperature (K)
μ_c	critical sticking viscosity (kg/m-s)
μ_p	particle viscosity (kg/m-s)
ρ	density (kg/m^3)
σ_{SB}	Stefan-Boltzmann constant $\left(5.67 \times 10^{-8} \frac{W}{m^2 K^4}\right)$
$\vec{\tau}$	stress tensor vector

Subscripts

g	denotes gas phase
H	denotes high temperature
i, j	denotes arbitrary species
L	denotes low temperature
p	denotes particle

Elements and Compounds

Al	aluminum
Al_2O_3	aluminum oxide
B	boron
Ca	calcium
CaO	calcium oxide
Cr	chromium
Fe	iron
Fe_2O_3	iron oxide
Ge	germanium
K	potassium
K_2O	potassium oxide
MgO	magnesium oxide
Na	sodium
Na_2O	sodium oxide
NO_x	nitrous oxides (x can range from 1 to 3)
P	potassium
Si	silicon

SiO_2	silicon dioxide
Ti	titanium
TiO_2	titanium dioxide

Acknowledgements

I would first like to express my gratitude to my graduate academic advisor over the course of the past three years, Dr. Gautham Krishnamoorthy. Dr. Krishnamoorthy encouraged me to pursue the combined BS/MS degree at the University back in the fall of 2019. I began doing research under his guidance in 2020. Since then, I have learned invaluable information regarding how to approach scientific research, as well as an onslaught of topics relevant to my thesis. He has also been kind enough to share job openings with me, which has given me a good idea of how I can apply the knowledge I've learned through this research to a career after graduation. He has been an incredible mentor for me in both my undergraduate and graduate academic career, and I will be forever thankful for him.

Next, I would like to thank Dr. Wayne Seames. I got to know Dr. Seames in my senior year of undergraduate courses, where he taught Process Controls and Plant Design. I have learned valuable information about the chemical engineering industry as a whole through his lectures and stories from his life. I am very grateful to have someone with his experience and expertise in the industry on my committee.

I would also like to thank Dr. Steve Benson for agreeing to be on my committee. Dr. Benson is the CEO of Microbeam Technologies, Inc (MTI). This project was a joint effort between UND and MTI. The field measurements made by MTI drove the simulation focus of this project. Throughout the past three years, I have learned much about coal combustion and ash deposition from listening to Dr. Benson speak in our meetings with Microbeam. I am thankful to have him on my committee. His expertise in fuel combustion has been a big help in my research.

Lastly, I would like to thank my parents, family, and friends. Their continued support throughout my six years at UND has made this a worthwhile experience in my academic journey, and for that I am forever thankful.

This work was funded by the US Department of Energy (Grant Number: DE-FE0031741). Any opinions, findings, and conclusions or recommendations contained in this material are those of the author and do not necessarily reflect the views of the US Department of Energy.

Abstract

Today, a significant number of coal-fired power plants are required to decrease the operating load as a result of intermittent power availability from wind or solar sources. Low load conditions introduce a number of challenges for these plants, such as decreased efficiency and degradation of system components due to cycling. Ash deposition on heat transfer surfaces makes these problems even worse. The overall goal of this project is to improve the understanding of fireside ash deposition behavior as the load fluctuates, thereby allowing for more efficient operations.

To accomplish this goal, a computation fluid dynamic (CFD) based simulation methodology was developed and refined to match field test measurements of deposition rates at 33%, 75%, and 100% load conditions in a cyclone fired boiler burning a North Dakota lignite coal. The deposition rate measurements were taken between the secondary superheater and reheater sections of the boiler. These measurements showed a significant reduction in deposition rates during with a decrease in operational load. The primary objective in this study was to discover the mechanisms behind these observations.

First, operational data from the power plant was used to carry out simulations of the full boiler. Simulations were carried out to match gas temperatures and velocities within the boiler. Decoupled simulations of the ash deposition process in the vicinity of the secondary superheater were carried out once the gas temperatures and velocities were confirmed to be adequately represented. This corresponded to the location where the deposition measurements were taken. The results of these decoupled simulations showed that in addition to the gas velocities and temperatures, the fly-ash particle size distribution (PSD) and their composition and concentration

were all important variables in deposition rate predictions. Assuming an ash partitioning of 50% - 50% between the slag and fly-ash at the cyclone and a reasonable estimate of the fly-ash PSD (from literature), a critical viscosity and particle kinetic energy (PKE) based capture criterion, the trends in the measured deposition rates were predicted successfully. In addition, the mass flow rates of fly-ash in the size range of 10 to 30 microns was determined to be critical. This was the size range of particles where the most significant increase of impaction efficiencies occurred by inertial impaction.

The next goal was to ascertain if the assumed ash partitioning ratio and the fly-ash PSD that resulted in match to the deposition rate measurements could be predicted using well-resolved simulations of the cyclone barrel. Plant operational data of the cyclone flow rates encompassing the load conditions 50% – 100% were employed to simulate combustion within a single cyclone barrel in the boiler. First, the sensitivity of different modeling parameters on the combustion characteristics within the cyclone were investigated in the absence of any particle capture criterion at the cyclone walls (that is no ash being captured in the slag layer). These results showed that the gas temperatures at the cyclone barrel outlet were only mildly sensitive (roughly within 150 K) to the heterogeneous char combustion modeling methodology. A decrease in load resulted in higher residence times for particles inside the cyclone barrel. This is likely attributed to more swirling of the particles caused by lower gas velocities. Variations in the parent fuel PSD did not impact the outlet gas temperature or char burnout significantly.

Next, the particle kinetic energy – particle viscosity based capture criterion was modified to account for the highly swirling turbulent flow within the cyclone barrel to predict the ash portioning. The PSD at the cyclone outlet and the percent of total ash captured in the slag layer were close to initial estimates employed in the decoupled ash deposition calculations. The ash

partitioning did not vary significantly across different cyclone loads when employing the shrinking sphere heterogeneous combustion model and their magnitude (~50%) was in line with previous field observations for this parent fuel ash composition.

Chapter 1 - Introduction

1.1 Motivation

Coal power plants have been supplying power for homes and factories since the mid-1880s [1]. In the United States, 22% of electricity was generated by coal in 2021 [2]. With such a large fraction of the nation's electricity production, it is important to understand what is happening during operation of a coal boiler. With the emergence and increased usage of renewable energy sources, coal production has decreased. In the US, the average annual net generation from coal sources reached an annual high of 2 billion kilowatt-hours (kWh) and fell to 1.2 billion kWh in 2016 [3].

With a decrease in demand for coal powered electricity, power plants cannot always operate at full load conditions. These plants face new challenges associated with decreased efficiency during low load conditions as well as degradation of system components due to cycling. In addition, previous studies have found that decreasing the load introduces maldistributions in temperature and velocity, which can cause thermal and mechanical stress on heat exchanger tubes, as well as reduced heat transfer [4,5]. Ash deposition on the heat transfer surfaces also plays a crucial role in increasing the severity of these problems. The overall goal of this project is to improve our understanding of fireside ash deposition behavior under a range of load conditions thereby allowing for more efficient operations.

To meet this objective, a computational fluid dynamic (CFD) based simulation methodology was developed and refined in an attempt to match field measurements of deposition rates made at 33%, 75% and 100% load conditions in a cyclone fired boiler burning a North Dakota lignite coal. The deposition rate measurements, (made by our project partner Microbeam

Technologies Incorporated, or MTI) which were made between the secondary superheater and reheater sections, showed a significant reduction in deposition rates during low load operations. The primary goal in this study was to uncover the mechanisms behind these observations.

This project focuses on a cyclone-fired coal boiler burning a North Dakota lignite coal. Here, the combustion of the coal particles occurs in cyclone barrels, which feed into the boiler, as shown in Figure 1.1.

First, operational data from the power plant was used to carry out simulations of the full boiler. Strong swirling flow features (anisotropic turbulence) occurs within the cyclone barrels, presenting numerical challenges in converging these simulations. Simulations of a cyclone fired coal boiler are generally performed in a decoupled manner, with the cyclone and boiler simulations performed separately. The flow exiting the cyclone is then entered as an input boundary condition for the boiler. However, since cyclones are operated in a fuel-rich mode to reduce the formation of NOx, such a methodology introduces additional challenges related to accurate tracking of any unburnt fuel exiting the cyclone. To mitigate these challenges, this project covers a handful of studies to successfully accomplish an end-to-end simulation of a coal particle from the cyclone inlet to the boiler exit. This is done through a careful selection of mesh size and simulation parameters for a range of load conditions.

Simulations were carried out to match gas temperatures and velocities within the boiler. Decoupled simulations of the ash deposition process on a deposit probe were carried out by our project team once the gas temperatures and velocities were confirmed to be adequately represented. These decoupled simulations were deemed to be necessary to enable the use of a very fine mesh in the region where the deposition measurements were taken. The results of these decoupled simulations showed that in addition to the gas velocities and temperatures, the fly-ash

particle size distribution (PSD) and their composition and concentration were all important variables in deposition rate predictions. Assuming an ash partitioning of 50% - 50% between the slag and fly-ash at the cyclone and a reasonable estimate of the fly-ash PSD (from literature), a critical sticking viscosity and particle kinetic energy (PKE) based capture criterion allowed for adequate representation of measured deposition rates given by MTI. In addition, the mass flow rates of fly-ash in the size range of 10 to 30 microns was determined to be critical. Most of the effort in this thesis was focused on determining if the fly-ash mass partitioning and fly-ash PSD (that matched the measured deposition rates) could be predicted using highly resolved simulations of the cyclone instead of being specified as needed for the boiler.

However, since many of the important parameters needed to model the cyclone successfully are not measured or monitored, reasonable estimates of these needed to be made. To meet this goal, the second portion of this thesis summarizes the impact of different modeling parameters in ANSYS Fluent, which were fuel inlet PSD, heterogeneous combustion model, and particle capture within the cyclone barrel on the simulation results. Previous experience in this project has shown that these are likely the most important parameters or variables impacting carbon burnout, fly-ash mass partitioning, and fly-ash PSD predictions exiting the cyclone.

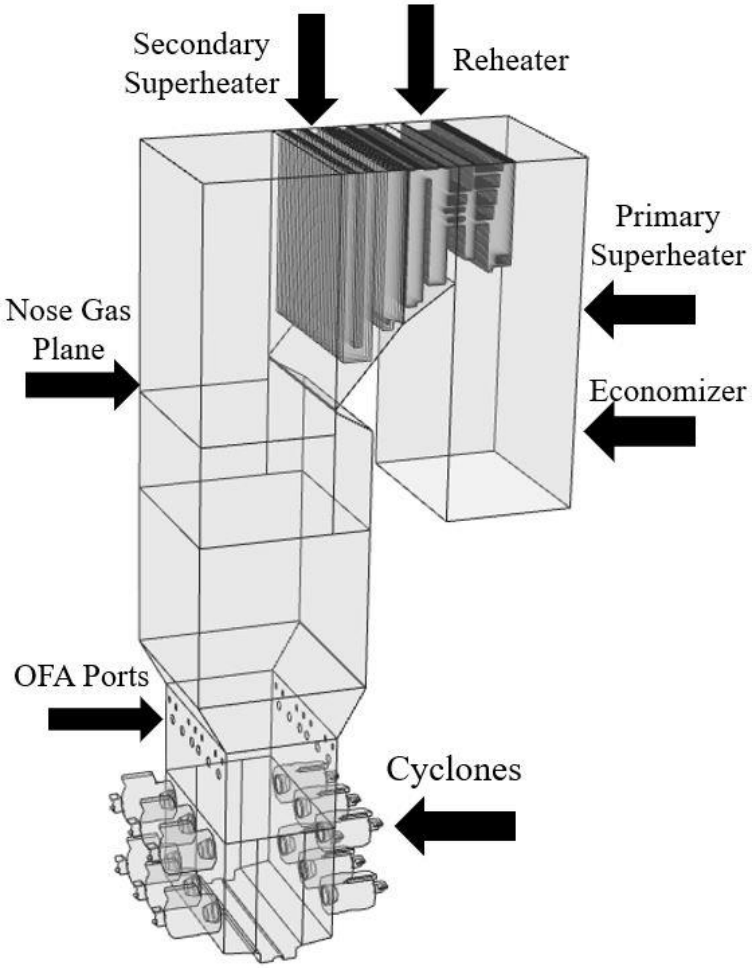

Figure 1.1. Geometry of the Full Boiler with Twelve Cyclones

1.2 Thesis Outline

The simulations were carried out using the computational fluid dynamics (CFD) software ANSYS Fluent (version 19). The remainder of this thesis is separated into six chapters. Chapter 2 provides an overview of the combustion modeling methodology in ANSYS Fluent. Chapter 3 summarizes the results from the full boiler at four loads (33%, 50%, 75% and 100%) along with results from the decoupled deposition rate calculations. Chapter 4 explores the effects that a char combustion model, load, and coal type have on flow characteristics at the outlet of the cyclone barrel. Chapter 5 assesses the impact of the inlet fuel particle size distribution (PSD) on the flow

characteristics at the outlet of a cyclone barrel. Chapter 6 focusses on the impact of the particle capture model along the cyclone walls. The final chapter (Chapter 7) provides overall conclusions for the aforementioned chapters, as well as recommendations for future work.

References

[1] Dec 22, 2020 by POWER. "History of Power: The Evolution of the Electric Generation Industry." *POWER Magazine*, 23 Dec. 2020,

https://www.powermag.com/history-of-power-the-evolution-of-the-electric-generation-industry/.

[2] "Frequently Asked Questions (Faqs) - U.S. Energy Information Administration (EIA)." *Frequently Asked Questions (FAQs) - U.S. Energy Information Administration (EIA)*,

https://www.eia.gov/tools/faqs/faq.php?id=427&t=3.

[3] "Most Coal Plants in the United States Were Built before 1990." *Most Coal Plants in the United States Were Built before 1990 - Today in Energy - U.S. Energy Information Administration (EIA)*,

https://www.eia.gov/todayinenergy/detail.php?id=30812.

[4] Ryno Laubscher, Pieter Rousseau, CFD study of pulverized coal-fired boiler evaporator and radiant superheaters at varying loads, Applied Thermal Engineering, Volume 160, 2019, 114057, ISSN 1359-4311,

https://doi.org/10.1016/j.applthermaleng.2019.114057

[5] Majdak, Marek, and Sławomir Grądziel. "Influence of Thermal and Flow Conditions on the Thermal Stresses Distribution in the Evaporator Tubes." *Energy*, vol. 209, 2020, p. 118416.,

https://doi.org/10.1016/j.energy.2020.118416.

Chapter 2 – Background

2.1 Coal Combustion

As coal is heated, the organic material within is pyrolyzed. The remaining solid mixture is comprised of carbon and minerals, which is known as char. Coal combustion is mainly the combustion of carbon and the volatiles within the coal. This combustion process can be broken down into three steps. The first is the release of volatile matter from the coal. The second is the oxidation of that volatile matter. Lastly is the burning of the char.

During the devolatilization stage, moisture present in the coal will vaporize as it is heated. As the temperature continues to rise, hydrocarbon gases and tarry substances are emitted. Devolatilization can take as little as mere milliseconds or as high as several minutes to complete.

Char burnout is the process of carbon being oxidized and burned by the hot oxygen gas following the devolatilization of the coal particles. These particles are porous, so the gaseous oxygen diffuses to the pore surfaces. This is a heterogeneous process that can take seconds to several minutes depending on the size and porosity of the coal particle [1]. The primary reactions in the char combustion process are shown in Table 2.1.

Table 2.1. Primary Reactions During Char Combustion [1]

Reaction	Heat of Reaction (kJ)
$C + O_2 \rightarrow CO_2$	-392.9
$C + ½\ O_2 \rightarrow CO$	-111.2
$CO + ½\ O_2 \rightarrow CO_2$	-281.7
$C + CO_2 \rightarrow 2CO$	170.5

2.2 CFD Framework

Dispersed, multiphase flow occurs when there are one or more phase(s) in the form of particles, droplets, or bubbles that are contained within a continuous carrier phase (liquid or gas).

For this thesis, the dispersed, multiphase flow is a particle phase (coal) entrained in the continuous carrier phase (oxidizing gas/flue gas). There are two ways to model these flow fields. The first being a Euler-Euler approach and the second being a Euler-Lagrange approach. This thesis used the Euler-Lagrange approach for all numerical simulations. An explanation of the Euler-Lagrange approach is contained in the following paragraphs.

ANSYS Fluent is a computational fluid dynamics (CFD) software. CFD uses numerical methods to solve approximate solutions relating to fluid dynamics and heat transfer. Outside of very simple solutions, CFD uses partial differential equations to solve for the fluid flow and heat transfer by employing numerical methods [2]. This fluid phase is treated as a continuum by solving the Navier-Stokes equations, while the solid phase is solved by tracking a large number of particles through the flow field. The solid phase is able to exchange momentum, mass, and energy with the fluid phase.

ANSYS Fluent utilizes a Lagrangian discrete phase model (DPM), which follows the Euler-Lagrange approach. A primary assumption of this model is that the solid phase occupies a low volume fraction, even if the mass flow rate is higher relative to the fluid phase. The particle paths are computed individually at specified intervals during the fluid phase calculations. These are known as DPM updates in ANSYS Fluent [3].

The governing equation for the conservation of mass (continuity equation) in the continuous fluid phase is shown in equation 2.1 [4]:

$$\frac{\partial \rho}{\partial t} + \nabla \cdot (\rho \vec{v}) = S_m \qquad 2.1$$

where ρ is the density of the fluid, $\rho\vec{v}$ is a mass flux vector, and S_m is a source term for the addition of mass from the discrete solid phase to the continuous fluid phase. The governing equation for the conservation of momentum is shown in equation 2.2 [3]:

$$\frac{\partial}{\partial t}(\rho\vec{v}) + \nabla \cdot (\rho\vec{v}\vec{v}) = -\nabla p + \nabla \cdot (\vec{\tau}) + \rho\vec{g} + \vec{F} \qquad 2.2$$

where the first term of the equation is the rate of change of momentum per unit volume. The second term is the rate of momentum addition due to convection per unit volume. The static pressure is denoted as p. The second term on the right-hand side of equation 2.2 is the rate of momentum addition due to molecular transport per unit volume. The stress tensor is denoted as $\vec{\tau}$. The gravitational body force is $\rho\vec{g}$ and $\vec{F}$ is an external body force. The governing equation for the conservation of energy in the continuous fluid phase is shown in equation 2.3 [4]:

$$\frac{\partial}{\partial t}(\rho E) + \nabla \cdot \left(\vec{v}(\rho E + \rho)\right) = \nabla \cdot \left(k_{eff}\nabla T - \sum_j h_j \bar{J}_j + \left(\vec{\tau}_{eff} \cdot \vec{v}\right)\right) + S_h \qquad 2.3$$

where the first term in equation 2.3 is the rate of change of energy per unit volume. The second term is the energy transfer due to convection, k_{eff} is the effective thermal conductivity, which is the sum of the thermal conductivity (k) and the turbulent thermal conductivity (k_t). The energy transfer due to conduction is $k_{eff}\nabla T$. $\bar{J}_j$ is the diffusion flux of species j. $\sum_j h_j \bar{J}_j$ is the energy transfer due to species diffusion. The energy transfer due to viscous dissipation is $\vec{\tau}_{eff} \cdot \vec{v}$. S_h is a source term which includes the heat of reaction and any other user-defined volumetric heat sources. The governing equation for the conservation of species in the continuous fluid phase is shown in equation 2.4 [4]:

$$\frac{\partial}{\partial t}(\rho Y_i) + \nabla \cdot (\rho\vec{v}Y_i) = -\nabla \cdot \vec{J}_i + S_i \qquad 2.4$$

where Y_i is the local mass fraction of species i. The first term in the equation is the rate of change of the mass fraction of species i. The second term is the convective transfer of species i. $\vec{J}_i$ is the diffusion flux of species i. R_i is the net rate of production of species i. S_i is a source term for the rate of production of species i through the addition of the discrete solid phase or any other user-defined sources. The equation for the discrete solid phase trajectory in a Lagrangian framework is shown in equation 2.5 [4]:

$$\frac{\partial \bar{u}_p}{\partial t} = F_D\left(\bar{u} - \bar{u}_p\right) + \frac{\bar{g}(\rho_p - \rho)}{\rho_p} + \bar{F} \tag{2.5}$$

where $\bar{u}_p$ is the ash particle velocity. F_D is the force of hydrodynamic drag and $\bar{u}$ is the fluid phase velocity. The first term in the equation is the hydrodynamic drag force per unit particle mass. The force of gravity is represented as $\bar{g}$. $\bar{F}$ is an additional acceleration term. The hydrodynamic drag, F_D, is calculated as [4]:

$$F_D = \frac{18\mu}{\rho_p d_p^2}\frac{C_D Re}{24} \tag{2.6}$$

where μ is the molecular viscosity of the fluid, C_D is the drag coefficient, and Re is the Reynolds number. The drag coefficient, C_D, is calculated as [4]:

$$C_D = \alpha_1 + \frac{\alpha_2}{Re} + \frac{\alpha_3}{Re^2} \tag{2.7}$$

where α1, α2, and α3 are all numerical values applicable over several ranges of Re, given by Morsi and Alexander [4, 5]. Re is calculated as [4]:

$$Re = \frac{\rho d_p |\bar{u}_p - \bar{u}|}{\mu} \tag{2.8}$$

ANSYS Fluent uses four heat and mass transfer relationships to numerically simulate the heat and mass transfer of the discrete solid phase. These four relationships are inert heating, inert

cooling, devolatilization, and surface combustion [4]. The energy balance relating particle temperature to the convective heat transfer and absorption/emission of radiation at the particle surface is shown in equation 1.9 [4]:

$$m_p C_p \frac{dT_p}{dt} = h_c A_{s,p}\left(T_\infty - T_p\right) + \varepsilon_p A_{s,p} \sigma_{SB}\left(\theta_R^4 - T_p^4\right) \quad 2.9$$

where m_p is the particle mass and C_p is the particle heat capacity. T_p is the particle temperature and h_c is the convective heat transfer coefficient. $A_{s,p}$ is the particle surface area. T_∞ is the ambient temperature of the continuous fluid phase. The particle emissivity is represented as ε_p. σ_{SB} is the Stefan-Boltzmann constant $\left(5.67 \times 10^{-8} \frac{W}{m^2 K^4}\right)$. θ_R is the radiation temperature.

2.2.1 Modeling Particle Capture

Several models with varying degrees of sophistication have been developed over the years to accurately represent the capture phenomena and have been the subject of recent reviews (Kleinhans et al. 2018b). In this study, a critical particle viscosity-based capture criterion was adopted, where the capture probability (P_{stick}) equals unity if the particle viscosity (μ_p) is lower than the critical viscosity ($\mu_{p,critical}$):

$$P_{stick} = 1 \text{ if } \mu_p \leq \mu_{p,critical} \quad 2.10$$

P_{stick} is zero otherwise. Based on three datasets using similar particle sizes, particle kinetic energy (PKE), and gas velocities associated with this study, the following relationship between PKE and critical viscosity ($\mu_{p,critical}$) proposed by Kleinhans et al. (2018b) was adopted:

$$\mu_{p,critical} = \frac{5 \times 10^{-12}}{PKE^{1.78}} \quad 2.11$$

In Figure 2.1, the sticking criterion (Equations 2.10 and 2.11) are represented as a function of particle viscosity (μ_p) and particle kinetic energy (PKE) is represented as a diagonal line defining the sticking and rebounding conditions.

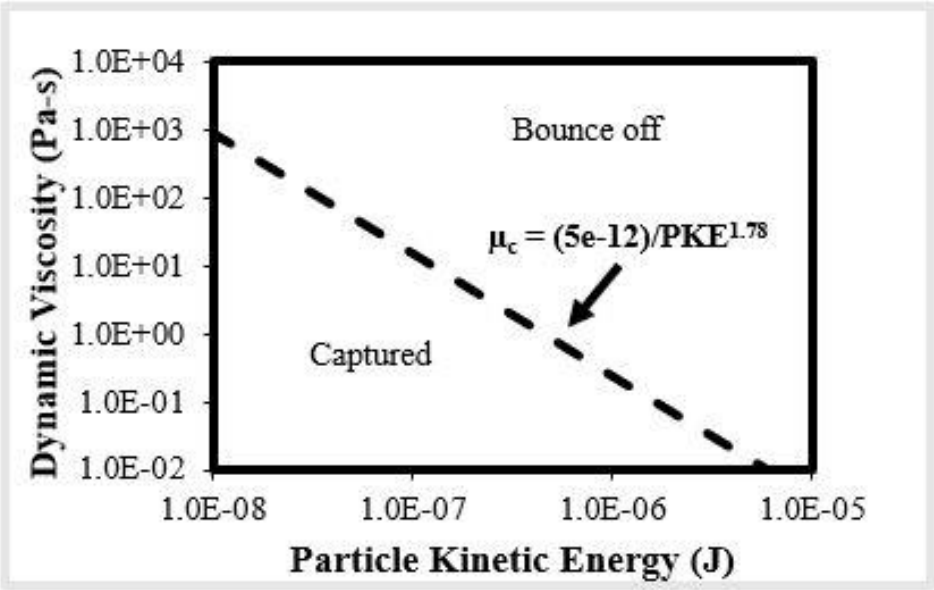

Figure 2.1. Particle Sticking Criterion as a Function of Particle Viscosity and Particle Kinetic Energy [6, 7]

In the high temperature region within the cyclone, the Urbain viscosity model parameters were employed to model the compositional and temperature dependencies of the particle viscosity. This model is introduced briefly here and discussed in more detail in Chapter 6. The particle viscosity μ_p (Pa-s) is a function of particle temperature, T_p, and two composition dependent model constants, "A" and "B"

$$\mu_p = \mathrm{A}\mathrm{T}_p \exp\left(\frac{1000B}{\mathrm{T}_p}\right) \qquad 2.12$$

The model constant "B" is calculated first, using the mass fractions of different metal oxide (M_xO_y) constituents of the ash (Urbain et al 1982):

$$B = \mathrm{f}\left(M_x O_y\right) \qquad 2.13$$

The model constant “A” is then estimated from “B” using a different functional form.

In the low temperature region following the secondary superheater, the Senior and Srinivasachar viscosity model parameters were employed to model the compositional and temperature dependencies of the particle viscosity. This model is introduced briefly here and discussed in more detail in Chapter 3. This model has the same functional form as the Urbain model discussed previously. The particle viscosity μ_p (Pa-s) is a function of particle temperature, T_p, and two composition dependent model constants, “A” and “B”

$$\mu_p = \mathrm{A}\mathrm{T}_p \exp\left(\frac{1000B}{\mathrm{T}_p}\right) \qquad 2.14$$

The model constant “B” is calculated first, using the mass fractions of different metal oxide (M_xO_y) constituents of the ash (Senior et al 1995):

$$B = \mathrm{f}\left(M_x O_y\right) \qquad 2.15$$

The model constant “A” is then estimated from “B” using a different functional form. The temperature dependence of the Urbain and Senior/Srinivachar viscosity models are shown in Figure 2.2.

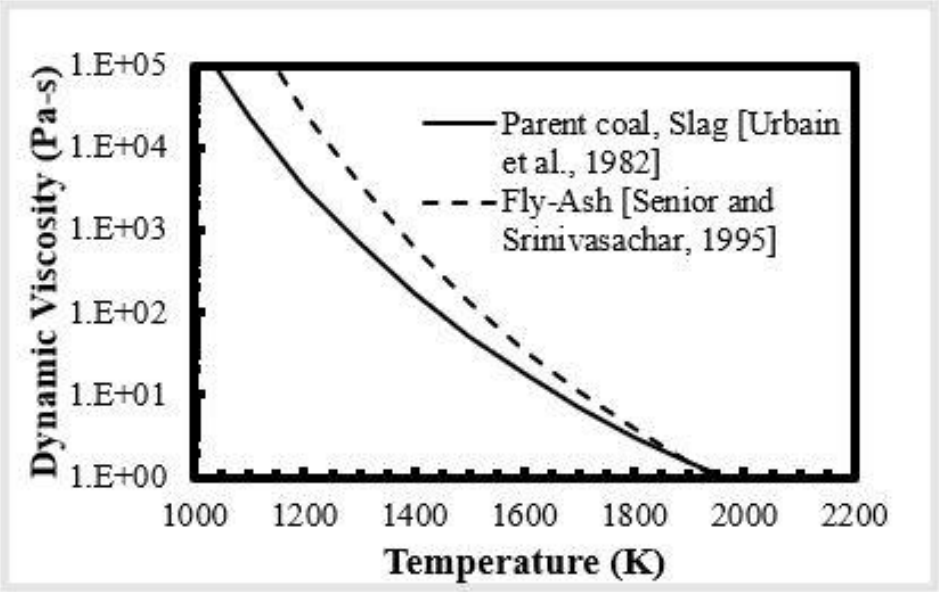

Figure 2.2. Temperature Dependence of Particle Viscosity Models [6, 7]

References

[1] Shen, Xianglin. "Coal Combustion and Combustion Products." *Coal, Oil Shale, Natural Bitumen, Heavy Oil and Peat*, edited by Gao Jinsheng, vol. 1, EOLSS Publications, 2009, pp. 319–339.

[2] Zikanov, Oleg. *Essential Computational Fluid Dynamics*. John Wiley & Sons, Inc., 2019.

[3] *Ansys Fluent 12.0 Theory Guide - 15.1 Introduction*, https://www.afs.enea.it/project/neptunius/docs/fluent/html/th/node239.htm.

[4] Ansys, Inc., Canonsburg, PA, USA. *Fluent User's Guide*, Release 2019 R2. (2019).

https://ansyshelp.ansys.com/

[5] S.A. Morsi and A.J. Alexander, “An investigation of particle trajectories in two-phase flow systems,” *J. Fluid Mech.*, vol. 55, no. 2, pp. 193-208, Sept. 1972.

[6] Kleinhans, U., Wieland, C., Frandsen, F.J., Spliethoff, H., 2018b. Ash formation and deposition in coal and biomass fired combustion systems: progress and challenges in the field of ash particle sticking and rebound behavior. Progr Energy Combust 68:65-168.

[7] Senior, C.L., Srinivasachar, S., 1995. Viscosity of ash particles in combustion systems for prediction of particle sticking. Energy Fuels 9 (2), 277-283

Chapter 3 - Effects of Load Variation in the Full Boiler

3.1 Abstract

With the increased demand and usage of renewable energy, coal power plants are fluctuating the loads they operate at. Operating at lower load conditions introduces some challenges for the boiler. This chapter analyzes temperature and velocity profiles within the boiler for four operational loads: 33%, 50%, 75%, and 100%. For low loads, this is generally accomplished by turning off select cyclones. Firstly, the gas temperatures at different sections of the boiler needed to be matched to boiler model estimations to ensure accuracy of results. The four areas of interest for this study were the nose gas plane, secondary superheater inlet, secondary superheater outlet, and the reheater outlet. ANSYS Fluent gas temperatures were in the range of 1000-1500 K for the nose gas plane, 900-1400 K for the secondary superheater inlet, 850-1250 K for the secondary superheater outlet, and 800-1000 K for the reheater outlet.

The coefficient of variation at these four areas and for all four loads were calculated to analyze any maldistributions that arose with lower loads. There were no identifiable trends for temperature maldistributions with variable operational loads.

The velocity profile was more uniform at higher loads, with higher velocity magnitudes as well. There was no trend for velocity maldistributions in the convective pass as the load fluctuated. The reheater outlet had high maldistributions, which is a result of the turn of the gas flow during the reheater section of the boiler.

A particle kinetic energy-based capture criteria to model ash deposition was able to give comparable trends to the measurements made by our project partner Microbeam Technologies

Incorporated (MTI). An increase in temperature (associated with higher loads) using this inertial impaction driven model led to a large increase in ash deposition rates.

3.2 Introduction

Coal power plants have been supplying power for homes and factories since the mid-1880s [1]. In the United States, 22% of electricity was generated by coal in 2021 [2]. However, with the emergence and increased usage of renewable energy sources, coal-based energy production has decreased. In the US, the average annual net generation from coal sources reached an annual high of 2 billion kilowatt-hours (kWh) and fell to 1.2 billion kWh in 2016 [3]. With a decrease in demand for coal powered electricity, power plants cannot always operate at full load conditions. These lower load conditions introduce some operational challenges. The purpose of this chapter will be to explore the effect that varying loads has on the boiler. Four different operational loads were used for this study: 33%, 50%, 75%, and 100%. Field test data given by MTI was given to ensure accuracy of results, as well as gas temperatures given by the power plant.

3.3 Materials and Methods

3.3.1 Full Boiler Geometry

A diagram of the full boiler is shown in Figure 3.1, with arrows signifying the general location of different sections. The over fire air (OFA) ports are placed above the twelve cyclone outlets. These ports aid in the combustion of the coal, as well as the reduction of NO_x formation. The cyclones operate at a higher-than-normal fuel to air ratio. Adding the OFA ports downstream of the cyclones allows for higher carbon conversion in the boiler, while limiting the formation of NO_x [4].

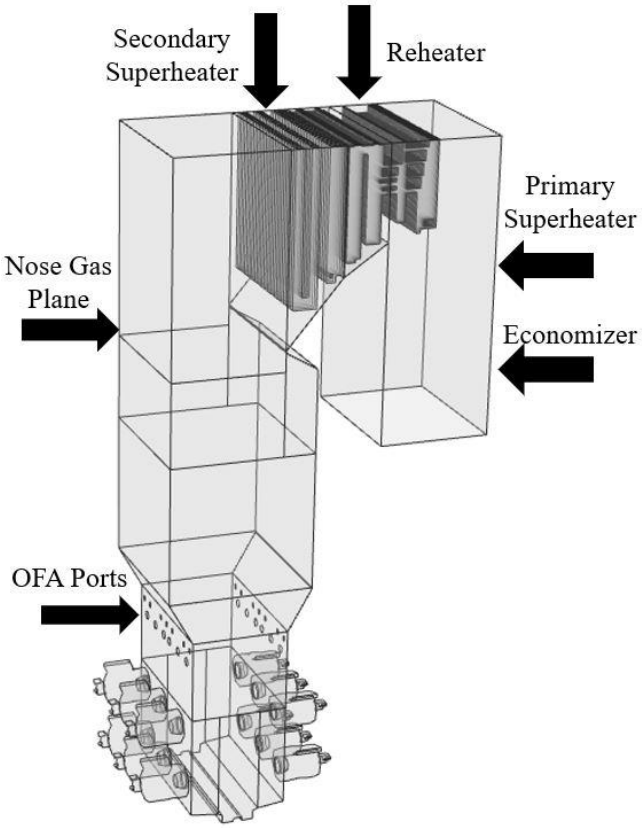

Figure 3.1. Full Boiler Diagram

The nose gas plane was an area used for temperature measurements by the plant. These were then compared to the simulation results in ANSYS Fluent, which will be discussed later. Possibly the most important region of the boiler is what's known as the convective pass. This region is comprised of the secondary superheater, reheater, primary superheater, and the economizer, which are shown in Figure 3.1. The purpose of the convective pass is to extract as much heat as possible from the flue gas. Several hundred heat exchanger tubes are located in the convective pass, with water flowing through them. This water is converted to steam when the flue gas travels through the convective pass. The steam produced travels to a turbine, which generates the electricity from the coal.

Operating at lower loads has been linked to high temperature gradients, especially in the convective pass [5]. This can lead to localized superheater tube overheating and insufficient heat

transfer in the convective pass. Non-uniform temperatures cause thermal stress on the superheater tubes. This can result in damage to the superheater tubes, leading to possible shutdowns for repair [6]. Operating at a low load can therefore decrease the time between required plant shutdowns for heat exchanger repairs. A maldistribution of temperature in the convective pass can lead to concentrated areas of ash deposition. Thermophoresis is a process where very small ash particles (<0.5 microns) are deposited on the surface of the heat exchange tubes due to a temperature gradient [7]. Having hot spots in the convective pass can cause large deposit growth in certain areas, which eventually will need to be manually removed.

3.3.2 Experimental Measurements of Gas Temperatures

To ensure accuracy of CFD simulations, matching flue gas temperatures at different sections of the boiler was vital. Flue gas temperatures were calculated using a model by the power plant. It solves equations simultaneously to calculate the gas temperatures. Firstly, the flue gas flow rate is calculated. This model depends on many important measurements, such as measured excess O_2, flue gas temperature at the economizer exit, assumed coal heating value, and the water and steam energy balance.

Using measured feedwater flow rates, as well as measured temperatures and attemperator spray flows, allows for calculation of the heat-duty of the whole boiler and each tube bank. Attemperators are used to control the steam temperature from the boiler or between boiler stages. It also imports the calculated reheat steam flow rate from a heat and mass balance, which computes an energy balance around the feedwater heaters to determine extraction steam flow rates. This model also does its own combustion stoichiometry calculations to determine flue gas composition from the measured excess O_2 and ultimate analysis coal composition, in addition to some minor effects such as unburned carbon in ash.

Using the above known flue gas flow rate and known water/steam side heat duty of each tube bank allows for back calculations of the required gas temperature difference across each tube bank for energy balance. That is how it gets from measured economizer outlet gas temperature to the measurement of furnace exit gas temperature and temperatures between each tube bank.

3.3.3 Ash Deposition Probe Simulations

Several models with varying degrees of sophistication have been developed over the years to accurately represent the capture phenomena and have been the subject of recent reviews [8]. There are two primary frameworks for modeling particle capture. The first is a molten fraction-based approach, where equilibrium calculations are performed to estimate the molten fraction and used in conjunction with a critical velocity [9]. In this study, a critical particle viscosity-based capture criterion was adopted, where the capture probability (P_{stick}) equals one if the particle viscosity (μ_p) is lower than the critical sticking viscosity ($\mu_{p,critical}$).

$$P_{stick} = 1 \text{ if } \mu_p \leq \mu_{p,critical} \quad 3.1$$

P_{stick} is zero otherwise. Based on three datasets using similar particle sizes, particle kinetic energy (PKE), and gas velocities associated with this study, the following relationship between PKE and critical viscosity ($\mu_{p,critical}$) proposed by Kleinhans et al. (2018b) was adopted:

$$\mu_{p,critical} = \frac{5\times10^{-12}}{PKE^{1.78}} \quad 3.2$$

This criterion has been validated for two previous studies. One of which is for ash deposition following combustion of a biomass and coal blend, while the other is ash deposition following pulverized coal. [10, 11] A PKE and particle viscosity criterion has been formulated

based on measurements in low velocity (<20 m/s) for non-swirling flows. Critical sticking viscosity is the point at which the slag changes from that of a Newtonian fluid to a plastic fluid upon cooling [12].

In Figure 3.2, the sticking criterion (Equations 3.1 and 3.2) are represented as a function of particle viscosity (μ_p) and particle kinetic energy (PKE) is represented as a diagonal line defining the sticking and rebounding conditions.

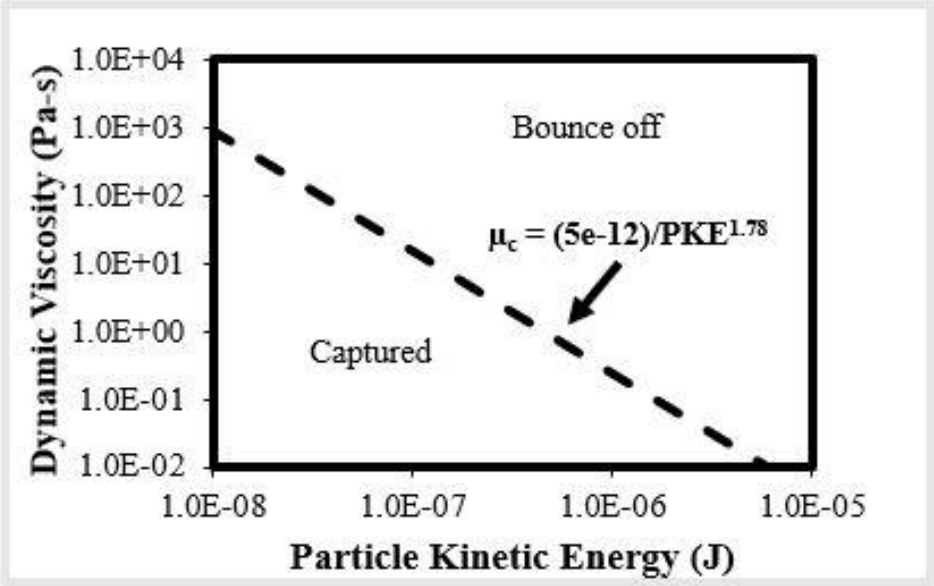

Figure 3.2. Particle Sticking Criterion as a Function of Particle Viscosity and Particle Kinetic Energy [8, 12]

This particle capture criteria is dominated by inertial impaction, which is considered as the most important mechanism that contributes significantly to the ash deposition build-up process. This process takes place when these particles, primarily with diameters greater than 10 microns, have adequate inertia to follow the gas flow and collide on the heat exchange surface by inertial forces [12].

In the region following the secondary superheater, the Senior/Srinivasachar viscosity model parameters were employed to model the compositional and temperature dependencies of the particle viscosity. This model is accurate for predicting particle viscosities at lower temperature regions, such as the convective pass of the boiler. This model describes the ash particle like a polymer, which is made up of a basic building block: the SiO_4^{4-}anion [14]. A network structure is formed as a result of strong covalent bonds between silicon and oxygen. The glassy silica network allows for several different cations. These fall into three categories, depending on their interaction within the network, glass formers, network modifiers, and amphoteric ions. Glass formers create the basic anionic polymer unit. Network modifiers disrupt the polymer chains by bonding with oxygen and terminating those chains. Amphoterics can act as either glass formers or network modifiers. These three categories are shown in Table 3.1.

Table 3.1. Senior/Srinivasachar Viscosity Model Cation Categories [14]

Classification	**Ion**
Glass Former	Si^{4+}, Ti^{4+}, P^{5+}
Network Modifier	Na^{+}, K^{+}, Ca^{2+}, Fe^{2+}, Mg^{2+}
Amphoteric	Al^{3+}, B^{3+}, Fe^{3+}

Modifier ions disrupt the glass structure, which tends to lower particle viscosity. Amphoteric ions can act as glass formers when combined with network modifier ions, which balance their charge and allows for the formation of stable metal oxide anion groups that can fit into the silicate network. However, if an insufficient number of modifier ions are present in the glass, amphoteric cations such as Al^{3+} and Fe^{3+} can act as network modifier ions themselves. The parameter used to describe the behavior of the glass network is the ratio of nonbridging oxygens to tetrahedral oxgyens, which is denoted as NBO/T. This is calculated as follows:

$$NBO/_T = \frac{CaO+MgO+FeO+Na_2O+K_2O-Al_2O_3-FeO_3}{\frac{(SiO_2+TiO_2)}{2}+Al_2O_3+Fe_2O_3} \quad 3.3$$

Where the chemical formulas denote mole fractions of the specified oxide in the glass. The amount of network modifying ions in the ash has been corrected for the number of cations needed to stabilize the aluminate and ferrite ions. This viscosity model uses parameters A and B, which depend only on the ash composition. Constant α is used to describe the fraction of network modifiers and amphoterics. MO is the mole fraction of network modifiers and A_2O_3 is the mole fraction of amphoterics. N is the mole fraction of SiO_2 in the ash and T_p is particle temperature. The following set of equations gives the Senior/Srinivasachar particle viscosity for a range of temperatures:

$$\mu_p = \mathrm{A}\mathrm{T}_p \exp\left(\frac{1000B}{\mathrm{T}_p}\right) \quad 3.4$$

$$A = a_0 + a_1 B + a_2\, NBO/T \quad 3.5$$

This model was separated into low and high temperature data sets to solve for A. The high temperature data set solves for A as follows:

$$A_H = -2.81629 - 0.46341B - 0.35342\, NBO/T \quad 3.6$$

The low temperature data set is calculated as follows:

$$A_L = -0.982 - 0.902473B \quad when\ NBO/T \geq 1.3 \quad 3.7$$

$$A_L = 2.478718 - 0.902473B - 2.662091\, NBO/T \quad when\ 0.2 \leq NBO/T < 1.3 \quad 3.8$$

$$A_L = 9.223 - 0.902473B \times NBO/T \quad when\ 0.0 \leq NBO/T < 0.2 \quad 3.9$$

$$A_L = 9.223 - 0.902473B \quad when\ NBO/T < 0 \quad 3.10$$

$$B = b_0 + b_1\alpha + b_2\alpha^2 + b_3 N + b_4 N\alpha + b_5 N\alpha^2 + b_6 N^2 + b_7 N^2\alpha + b_8 N^2\alpha^2$$

$$+ b_9 N^3 + b_{10} N^3\alpha + b_{11} N^3\alpha^2 \quad 3.11$$

B was solved using a linear regression to solve for the constants in both the low and high temperature region. These constants are shown in Table 3.2. The temperature dependence of the Senior/Srinivasachar viscosity model is shown in Figure 3.3.

Table 3.2. Constants Used for Evaluation of B in the Senior/Srinivasachar Viscosity Model [14]

Constant	Low Temperature	High Temperature
b_0	-7563.46	-224.98
b_1	24431.69	636.67
b_2	-17685.4	-418.7
b_3	32644.26	823.89
b_4	-103681	-2398.32
b_5	74541.33	1650.56
b_6	-46484.8	-957.94
b_7	146008.4	3366.61
b_8	-104306	-2551.71
b_9	21904.63	387.32
b_{10}	-68194.8	-1722.24
b_{11}	48429.31	1432.08

Table 3.3 shows the ash composition in weight percent, which allowed for the calculation of ash viscosities using the Senior viscosity model.

Table 3.3. Ash Composition Used for Probe Simulations

Compound	Weight Percent
Na_2O	1.5
MgO	1.8
Al_2O_3	15
SiO_2	41
P_2O_5	0.60
SO_3	1.3
Cl	0.30
K_2O	0.50
CaO	28
TiO_2	0.10
Cr_2O_3	0.40
Fe_2O_3	8.6
BaO	1.1

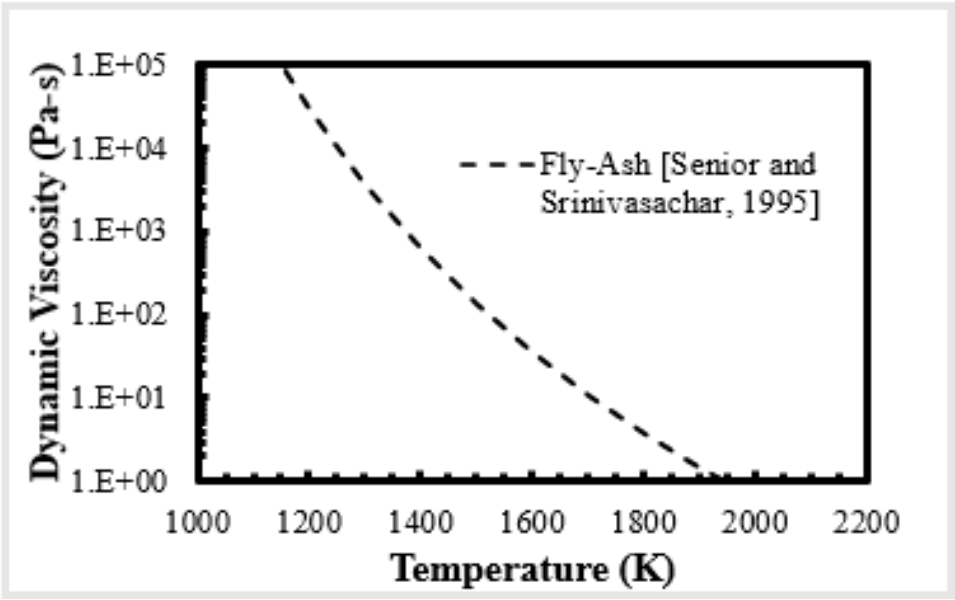

Figure 3.3. Temperature Dependence of Fly-Ash Viscosity Model [14]

The goal of this capture model was to match ash deposition rate trends given by MTI. Field tests were conducted using a metallic probe placed between the outlet of the secondary superheater and the inlet of the reheater. Tests were run under the following operational loads: 33%, 75%, and 100%. Figures 3.4 and 3.5 show the location of the probe used for these field tests and the geometry of the probe itself. The probe is placed at the entrance to a viewing port and allowed to sit in the boiler during operation. After a set amount of time, the probe is pulled out of the boiler and the deposits are scraped off and weighed. This allows for calculation of the deposition rates at different operational loads.

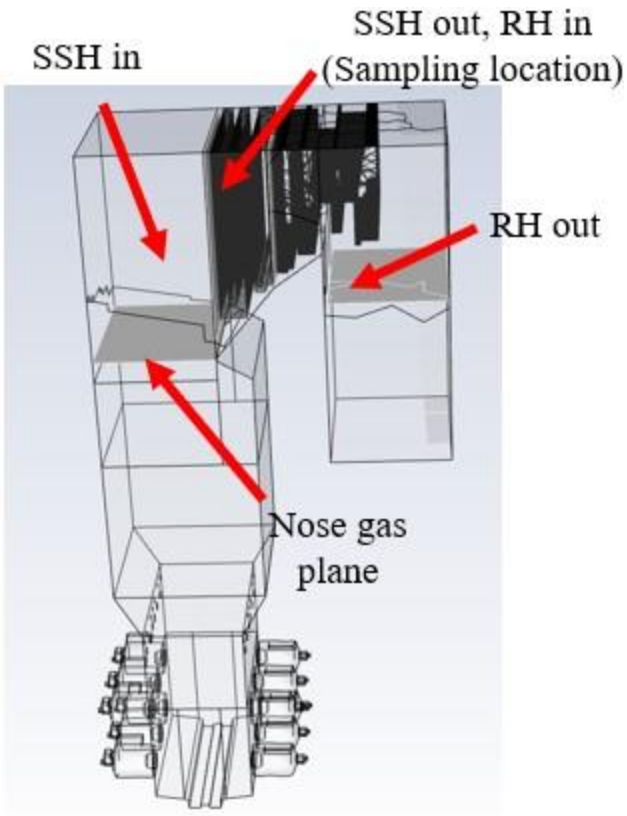

Figure 3.4. Location of Ash Deposition Probe

An important step in accurately representing ash deposition using CFD is calculating the impaction efficiency of ash particles hitting the surface being analyzed. Impaction efficiency is defined as the ratio of number of ash particles captured by the surface to the number of ash particles impacting the surface. The inertial impaction efficiency of particles on a cylinder can be expressed as a function of Stokes number [14]. Stokes number is a dimensionless number that characterizes the behavior of particles suspended in fluid flow. A lower number indicates the particle is subject to the path of the surrounding fluid, while a larger number indicates the particle is not influenced by the fluid. The equation for Stokes number is shown in Equation 3.12

$$St = \frac{\rho_p d_p^2 u_p}{9\mu_g d_c} \qquad 3.12$$

where ρ_p is particle density, d_p is particle diameter, u_p is particle velocity, μ_g is gas viscosity, and d_c is the diameter of the cylinder that the particles are impacting.

These values were taken from the full boiler simulations at the secondary superheater outlet. Diameter has the greatest effect on Stokes number. Stokes numbers in the range of 0.1 to 10 is where the most drastic increase in impaction efficiencies occur [9, 16]. This study used a particle size distribution with an average particle size of 28 microns. Figure 3.6 shows the distribution for the fly-ash as a Rosin-Rammler plot, which is a common way to represent pulverized coals. It shows the mass fraction of particles with diameter greater than a reference size. The formula for a Rosin-Rammler curve fit is shown in Equation 3.13 [15].

$$Y_D = \exp\left(-\left({}^{d}/_{\bar{d}}\right)^{n}\right) \tag{3.13}$$

where Y_D is the mass fraction of particles with diameter greater than d. The particle diameter is represented as d, in microns, and $\bar{d}$ is the mean particle diameter.

Figure 3.5. Probe geometry

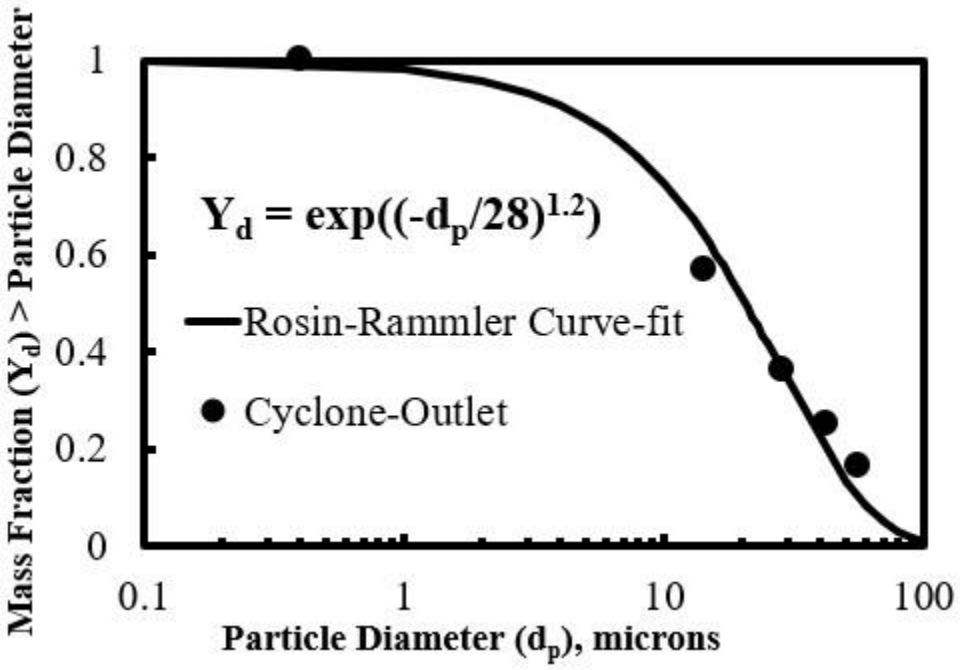

Figure 3.6. Fly-Ash PSD for Probe Simulations

Accurate predictions of the impaction efficiency using the Stokes number is only valid when the flow field near the deposition surface is accurately resolved [9]. For this study, that means to create a mesh with grid sizes of roughly 1 micron near the probe surface. This allows for an accurate depiction of the particle flow path as it nears the probe, thus minimizing any

numerical errors. This is shown in Figure 3.7, where the cell sizes become smaller closer to the probe surface. The cells are the shapes created by the intersecting gridlines. This is the mesh used for the numerical simulations of the ash deposition probe.

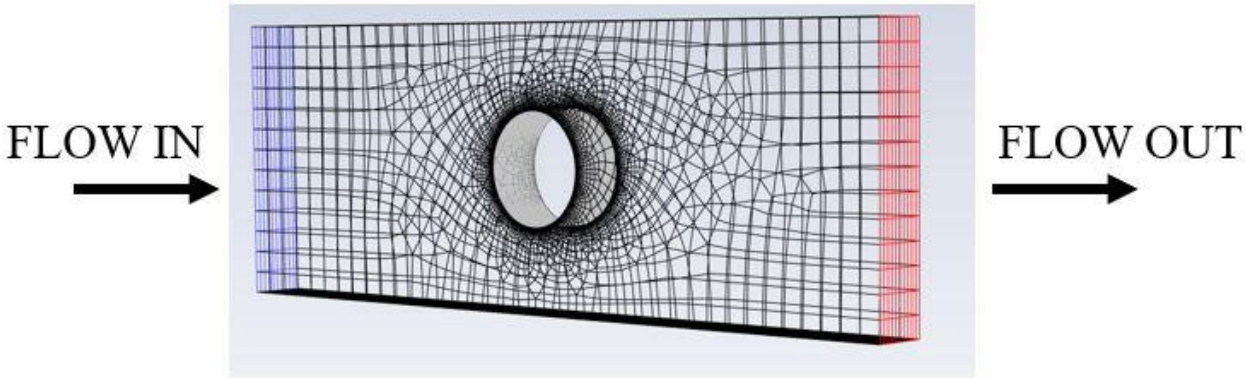

Figure 3.7. Probe Mesh Used in ANSYS Fluent

3.4 Results and Discussion

This chapter analyzes four operational loads, which are 33%, 50%, 75%, and 100%. These values correlate to different levels of energy output for the power plant. Figure 3.8 (a-d) show the simulation gas temperature results for the nose gas, secondary superheater inlet, secondary superheater outlet, and reheater outlet. The solid black line is the mean gas temperature from the numerical simulations. The standard deviation of the ANSYS Fluent results is represented by two dashed lines. Gas temperatures were in the range of 1000-1500 K for the nose gas plane, 900-1400 K for the secondary superheater inlet, 850-1250 K for the secondary superheater outlet, and 800-1000 K for the reheater outlet. It was hypothesized that gas temperatures would increase with an increase in load, which is supported by the ANSYS Fluent temperatures. ANSYS Fluent results show the expected temperature trends. The temperature should decrease moving from the nose gas to the reheater outlet. This is due to heat extraction from the superheater tubes. Numerical temperature results from ANSYS Fluent were in the

expected ranges predicted by the boiler model for all four loads (not shown here to maintain confidentiality).

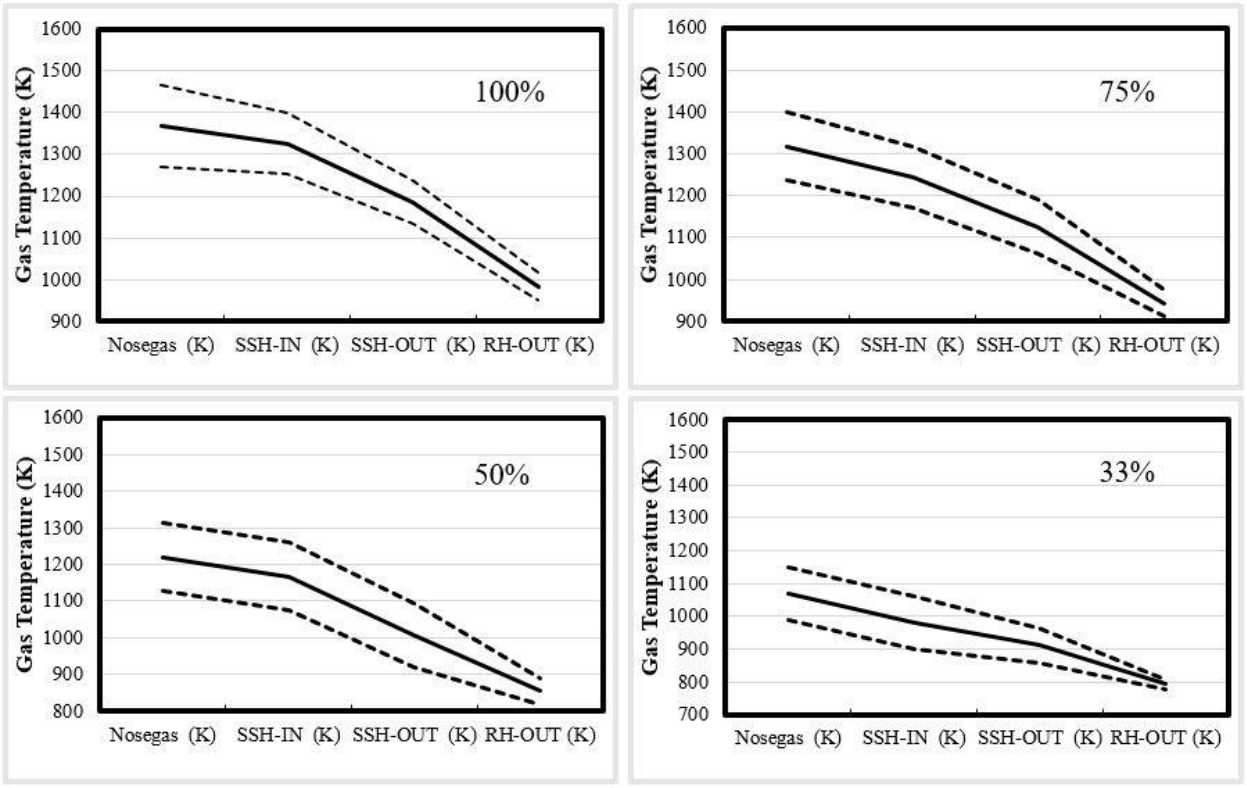

Figure 3.8 (a-d). CFD Estimations of Flue Gas Temperatures for All Four Loads

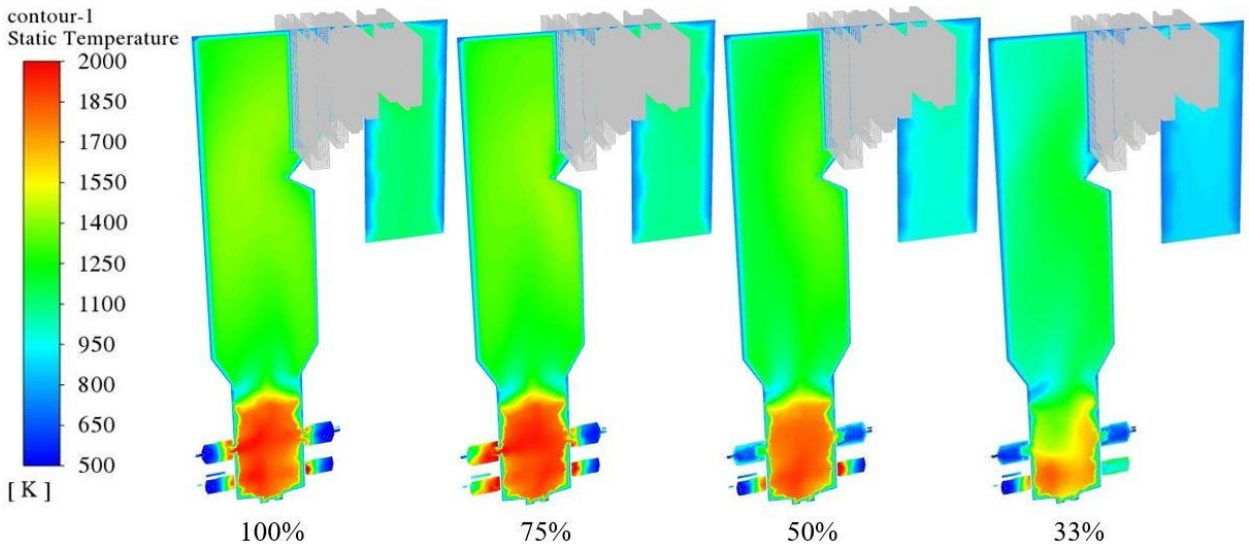

Figure 3.9. Full Boiler Temperature Contours for All Four Loads

The figures above show the gas temperature contours for the three loads. A temperature range of 500-2000 K was set for easier comparison across the loads. Warmer colors represent hotter gas temperatures. As the load is decreased, the temperature contour colors become cooler, indicating a decrease in gas temperatures in the boiler. Gas temperatures are hottest near the cyclones and over-fire air ports, with temperatures around 2000 K or higher.

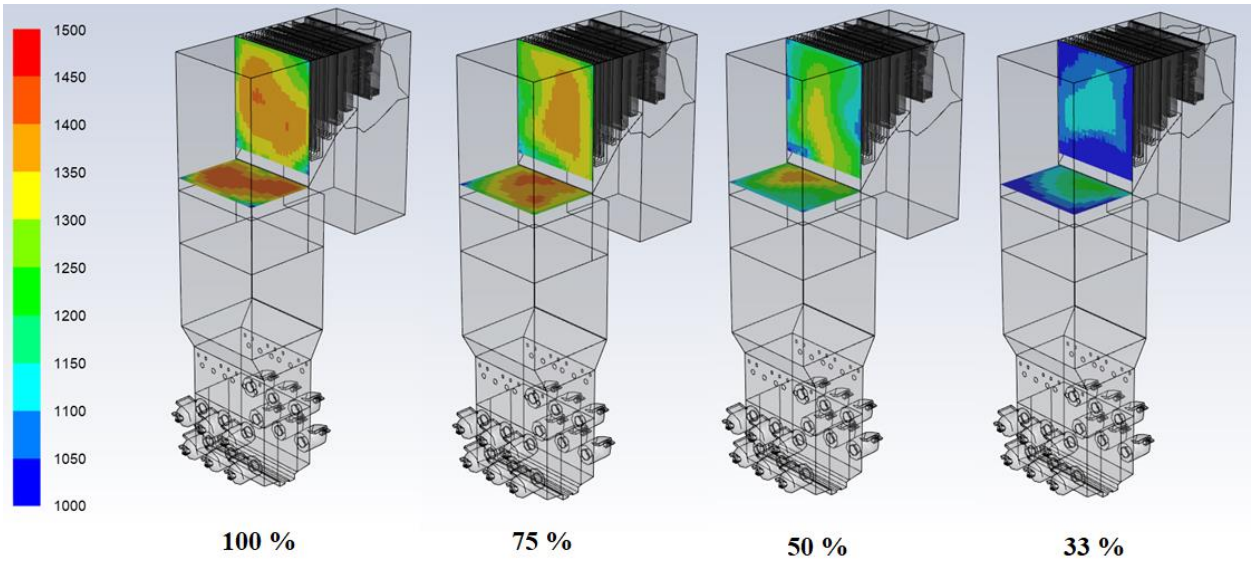

Figure 3.10. Nose Gas Temperature Contours for All Four Loads

Table 3.4. Coefficient of Variation of Gas Temperatures at Different Sections of the Boiler

Load	**100%**	**75%**	**50%**	**33%**
Nose Gas Plane	7.1E-02	6.2E-02	7.5E-02	7.7E-02
Secondary Superheater Inlet	5.5E-02	5.8E-02	8.1E-02	8.3E-02
Secondary Superheater Outlet	4.3E-02	5.7E-02	8.6E-02	5.8E-02
Reheater Outlet	3.4E-02	3.3E-02	4.2E-02	2.0E-02

Figure 3.10 shows the temperature contours at the nose gas section and the entrance to the secondary superheater for a range of 1000-1500 K. The primary interest was in identifying the temperature distribution as the load fluctuates. A uniform temperature distribution is desired. The nose gas planes show “hot spots” in temperature for all four loads. However, the temperature distribution appears to become slightly more uniform after the gas curves and enters the secondary superheater. To analyze this distribution of temperatures for the nose gas plane and convective pass, Table 3.4 was created, which displays the coefficient of variation of gas temperatures at each plane of interest in the boiler. Coefficient of variation, which is the standard deviation over the mean, is a measure of the variability from the mean value. In this case it is the variability from the mean gas temperatures. A higher coefficient of variation indicates a higher maldistribution of temperature, so in a truly homogeneous field, these values would all be zero. This table shows an increase in temperature maldistribution for the nose gas and secondary superheater inlet at 50% and 33% loads. However, these values may not be significant enough to present a real operational concern.

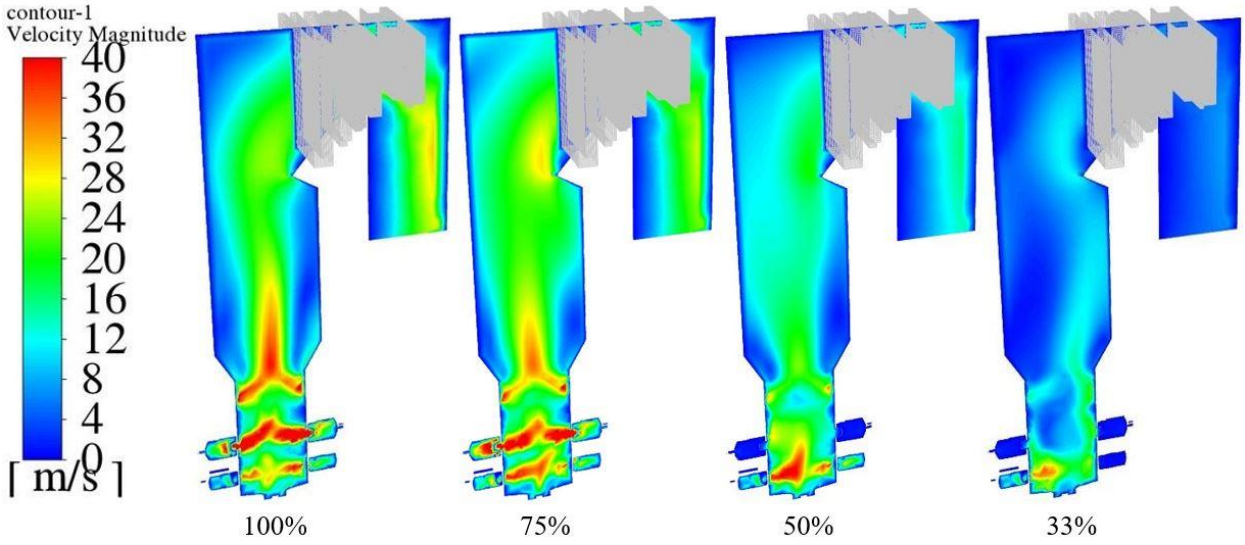

Figure 3.11. Full Boiler Velocity Contour for All Four Loads

Figure 3.11 shows the full boiler velocity profiles for the four loads, with a range of 0-40 m/s. A decrease in load results in a decrease in the velocity magnitude of the flue gas. As the load decreases, the velocity profile becomes less uniform. Residence time particle track figures were created in ANSYS Fluent to gain a better understanding of particle flow behavior in the boiler. This is shown in Figure 3.12, where particles with a diameter of 25 microns were tracked from the cyclone to the economizer outlet. 25 microns was roughly the average particle diameter used for the probe simulations, which was discussed earlier. As the load decreased, particle residence time increased due to a dip in the velocity magnitude of the flue gas, ranging from roughly 5 to 10 seconds when going from 100% load to a 33% load.

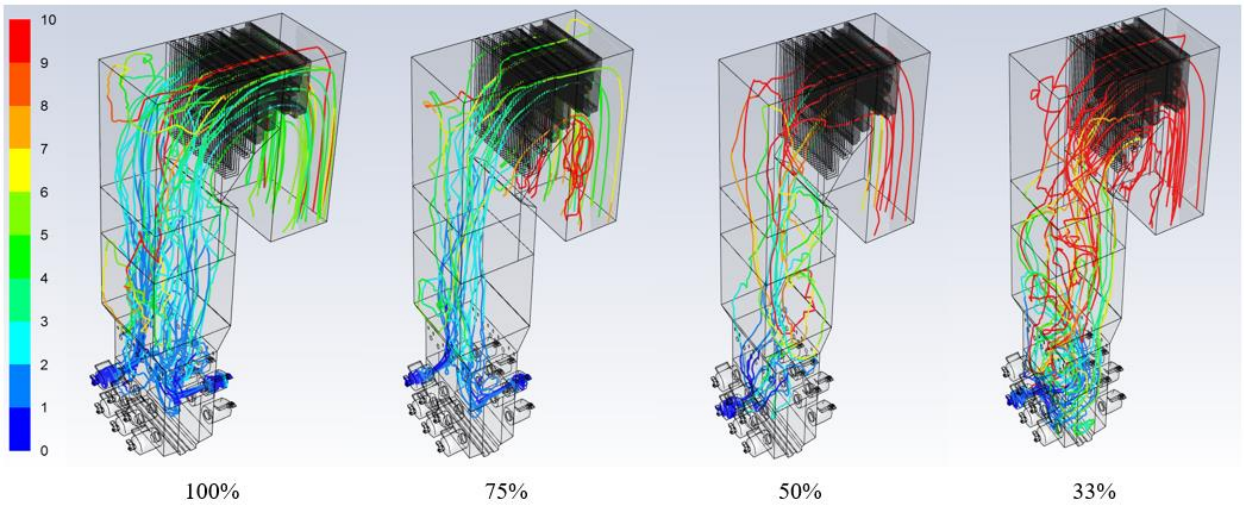

Figure 3.12. Particle Residence Time for 25 Micron Particles for All Four Loads

Figure 3.13 below shows the velocity contours at the nose gas plane and secondary superheater inlet for the four loads for a range of 0-34 m/s. Similar to the temperature contours discussed earlier, the primary focus was in identifying maldistributions for the velocity profile in the convective pass as the load fluctuates. The 75% and 100% load contours show some hot spots in these areas, while the 33% and 50% contours show a more uniform distribution of velocity magnitudes. However, when looking at this table here, there is no identifiable trend for velocity maldistributions as loads fluctuate. The reheater outlet had by far the greatest variation in velocity magnitudes when compared to the other sections. This is likely due to turbulence caused by the turn of the flow following the secondary and primary superheaters.

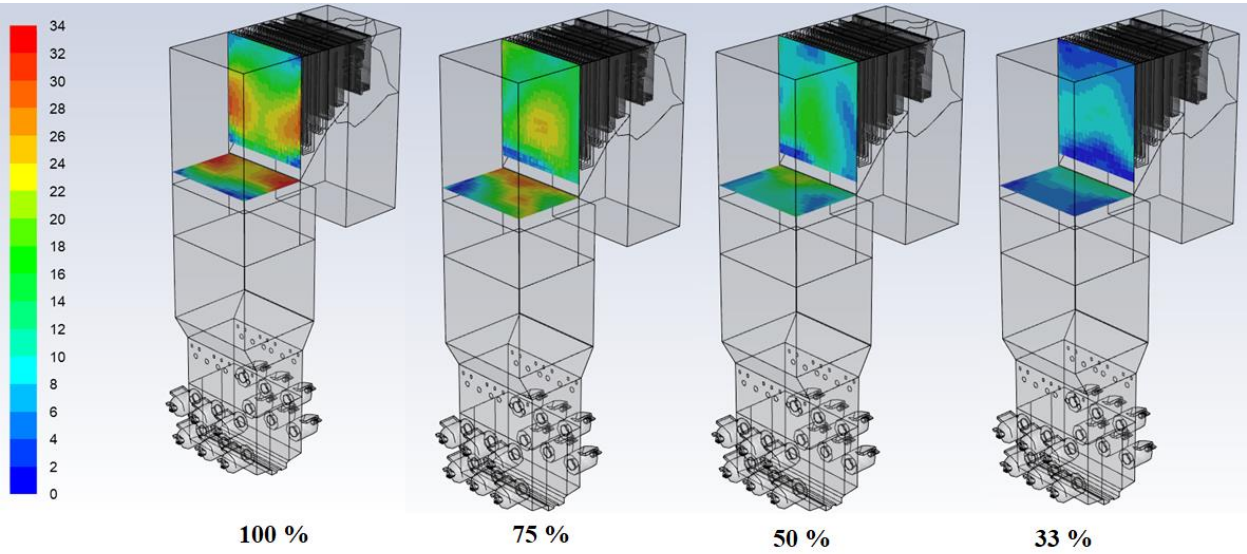

Figure 3.13. Nose Gas Velocity Contour for All Four Loads

Table 3.5. Coefficient of Variation of Gas Velocities at Different Sections of the Boiler

Load	**100%**	**75%**	**50%**	**33%**
Nose Gas Plane	0.39	0.37	0.36	0.37
Secondary Superheater Inlet	0.27	0.27	0.33	0.40
Secondary Superheater Outlet	0.26	0.29	0.27	0.34
Reheater Outlet	0.60	0.61	0.61	0.65

The first step in accurately predicting ash deposition rates was to ascertain the impaction efficiencies were being adequately represented as a function of the Stokes number. This was done for operational loads at 33%, 50%, and 75%, which is shown in Figure 3.14. The calculated impaction efficiencies from CFD results were in line with previous studies.

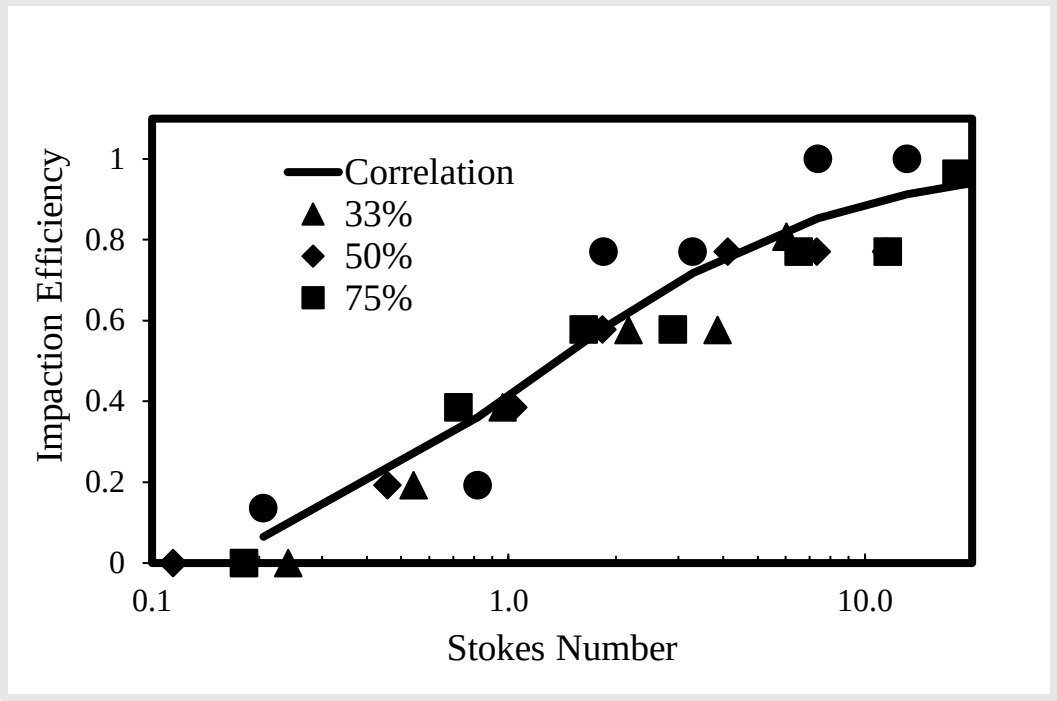

3.14. Numerical Predictions of Impaction Efficiency as a Function of Stokes Number

The next step was to compare deposition rates with the experimental measurements given by MTI. Deposition rates were given as a mass flux, which is the mass of deposits per surface area and time. These experimental and numerical results are shown in Figure 3.15. The CFD results are slightly higher than those collected by MTI. This is most likely due to the assumption for the CFD simulations of a clean probe. This means that the probe is always treated as a clean surface when a particle impacts it, regardless of if other particles have deposited prior. This model only accounts for inertial impaction onto a clean surface, so it overestimates actual deposition rates. Future studies should include deposit growth after the initial layer has formed, which can occur through several different mechanisms, such as thermophoresis, condensation, chemical reactions, and eddy impaction [13].

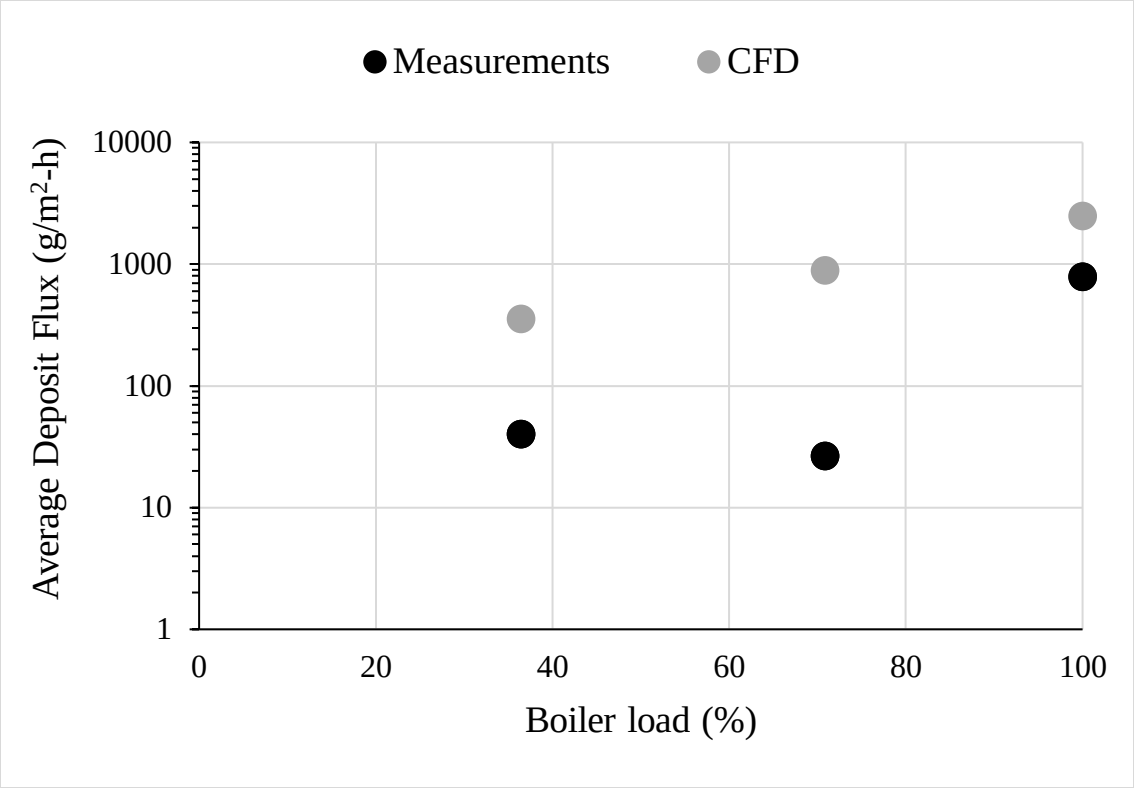

Figure 3.15. Experimental and Numerical Results for Ash Deposition Flux on Probe

Particle deposition rates increased with load using this model. This indicates that particle temperature and particle kinetic energy (PKE) are driving factors in ash sticking probability when using an inertial impaction deposition model. A higher particle temperature decreases the viscosity of the fly ash based on the Senior viscosity model. Gas temperature increases as the load is increased, which is shown in Figures 3.8 and 3.9. Higher gas temperatures are indicative of higher particle temperatures because the heat from the surrounding gas will diffuse to the fly ash particles. A higher particle kinetic energy is representative of higher flue gas velocities, which occur as the load is increased. As the load is increased, the particle kinetic energy increases and the viscosity of the fly ash particles decreases, which means the probability of the critical particle sticking viscosity being greater than the particle viscosity will drastically increase with an increase in operational load.

3.5 Conclusions

This chapter focused on gas temperatures and velocities within the full boiler. At higher loads, the gas temperatures exceed 2000 K near the over-fired air ports. There were four primary areas of interest for analyzing gas temperatures in the boiler: the nose gas plane, secondary superheater inlet, secondary superheater outlet, and the reheater outlet. ANSYS Fluent gas temperatures were in the range of 1000-1500 K for the nose gas plane, 900-1400 K for the secondary superheater inlet, 850-1250 K for the secondary superheater outlet, and 800-1000 K for the reheater outlet. These numerical results are in the expected range given by the boiler gas temperature model. Gas temperatures decreased with lower loads and as the flue gas moved through the convective pass, which is a result of heat extraction from the superheater tubes. Coefficient of variation at these four areas and for all four loads were calculated. The goal was to recognize any trends in temperature maldistributions. There were no identifiable trends for temperature and velocity maldistributions with load fluctuations that would present an operational concern. The velocity profile was more uniform at higher loads, with higher velocity magnitudes as well.

Particle deposition rates increased with load using the PKE-particle viscosity capture model. Particle temperature and PKE are driving factors for the ash sticking probability when using an inertial impaction deposition model. A higher particle temperature decreases the viscosity of the fly ash based on the Senior/Srinivasachar model. A higher particle kinetic energy is representative of higher flue gas velocities, which occur as the load is increased. As the load is increased, the particle kinetic energy increases and the viscosity of the fly ash particles decreases, which means the probability of the critical particle sticking viscosity being greater

than the particle viscosity will drastically increase with an increase in operational load. Future studies should include deposit growth after the initial ash layer is formed.

References

[1] Dec 22, 2020 by POWER. "History of Power: The Evolution of the Electric Generation Industry." *POWER Magazine*, 23 Dec. 2020, https://www.powermag.com/history-of-power-the-evolution-of-the-electric-generation-industry/.

[2] "Frequently Asked Questions (Faqs) - U.S. Energy Information Administration (EIA)." *Frequently Asked Questions (FAQs) - U.S. Energy Information Administration (EIA)*, https://www.eia.gov/tools/faqs/faq.php?id=427&t=3.

[3] "Most Coal Plants in the United States Were Built before 1990." *Most Coal Plants in the United States Were Built before 1990 - Today in Energy - U.S. Energy Information Administration (EIA)*, https://www.eia.gov/todayinenergy/detail.php?id=30812.

[4] Srivastava, Ravi K., et al. "Nitrogen Oxides Emission Control Options for Coal-Fired Electric Utility Boilers." *Journal of the Air & Waste Management Association*, vol. 55, no. 9, 2005, pp. 1367–1388., https://doi.org/10.1080/10473289.2005.10464736.

[5] Ryno Laubscher, Pieter Rousseau, CFD study of pulverized coal-fired boiler evaporator and radiant superheaters at varying loads, Applied Thermal Engineering, Volume 160, 2019, 114057, ISSN 1359-4311, https://doi.org/10.1016/j.applthermaleng.2019.114057

[6] Majdak, Marek, and Sławomir Grądziel. "Influence of Thermal and Flow Conditions on the Thermal Stresses Distribution in the Evaporator Tubes." *Energy*, vol. 209, 2020, p. 118416., https://doi.org/10.1016/j.energy.2020.118416.

[7] Lee, B. "Computational Study of Fouling Deposit Due to Surface-Coated Particles in Coal-Fired Power Utility Boilers." *Fuel*, vol. 81, no. 15, 2002, pp. 2001–2008., https://doi.org/10.1016/s0016-2361(02)00127-8.

[8] Kleinhans, U., Wieland, C., Frandsen, F.J., Spliethoff, H., 2018b. Ash formation and deposition in coal and biomass fired combustion systems: progress and challenges in the field of ash particle sticking and rebound behavior. Progr Energy Combust 68:65-168

[9] Cai, Y., Tay, K., Zheng, Z., Yang, W., Wang, H., Zeng, G., Li, Z., Keng Boon, S., & Subbaiah, P. (2018). Modeling of ash formation and deposition processes in coal and biomass fired boilers: A comprehensive review. *Applied Energy*, *230*, 1447–1544. https://doi.org/10.1016/j.apenergy.2018.08.084

[10] Gautham Krishnamoorthy, “Modeling ash deposition and shedding during oxy-combustion of coal/rice husk blends at 70% inlet O2,” International Journal of Coal Science & Technology (2023) 10:27, https://doi.org/10.1007/s40789-023-00583-8

[11] Gautham Krishnamoorthy, “Aerodynamic Influences on the Outer Ash Deposition Rates during Oxy-Coal Combustion." Cleaner Chemical Engineering (2022), https://doi.org/10.1016/j.clce.2022.100057.

[12] Ye, Insoo, et al. “Influence of Critical Viscosity and Its Temperature on the Slag Behavior on the Wall of an Entrained Coal Gasifier.” *Applied Thermal Engineering*, vol. 87, 2015, pp. 175–184.,

[13] Senior, C.L., Srinivasachar, S., 1995. Viscosity of ash particles in combustion systems for prediction of particle sticking. Energy Fuels 9 (2), 277-283

[14] Cai, Y., Tay, K., Zheng, Z., Yang, W., Wang, H., Zeng, G., Li, Z., Keng Boon, S., & Subbaiah, P. (2018). Modeling of ash formation and deposition processes in coal and biomass fired boilers: A comprehensive review. *Applied Energy*, *230*, 1447–1544. https://doi.org/10.1016/j.apenergy.2018.08.084

[15] Ansys Fluent 12.0 user's guide - 23.3.13 using the rosin-rammler diameter distribution method. (2009, January). https://www.afs.enea.it/project/neptunius/docs/fluent/html/ug/node692.htm

[16] Weber, R., Schaffel-Mancini, N., Mancini, M., & Kupka, T. (2013). Fly ash deposition

modelling: Requirements for accurate predictions of particle impaction on tubes using RANS-based computational fluid dynamics. *Fuel*, *108*, 586–596. https://doi.org/10.1016/j.fuel.2012.11.006

Chapter 4 – Sensitivity of Combustion within the Cyclone to the Char Combustion Model

4.1 Abstract

A key step in predicting the partitioning of ash between the slag layer and fly-ash within the cyclone is correctly modeling the evolving PSD and particle densities. In addition, the particle PSD at the outlet of the cyclone is important to model the deposition process along the flow path downstream of the cyclone. During the combustion of pulverized coal, the particles shrink and become more porous. This chapter utilized two different modeling approaches. The first is what's known as shrinking core, where the coal particle retains its initial diameter, but the density decreases as it burns. The second model is shrinking sphere, where the coal particle shrinks, but the density remains constant during combustion. The goal of this chapter is to analyze the aerodynamics of the particles in the cyclone, especially under low load conditions with reduced air and fuel flow rates. To accomplish this, the PSD was fixed for all scenarios and there was no capture of the fly-ash particles within the cyclone. A high silica and low base to acid (B/A) ratio coal was chosen for this study.

The residence time in the cyclone varied between five to twenty seconds. The char combustion model and gas velocities have a great impact on the particle tracks. Lower gas velocities, which occur at lower loads, cause the particles to swirl more towards the back of the cyclone and increase their residence time. Since five to twenty seconds is a sufficiently long residence time to achieve complete combustion for a 100 micron diameter coal particle, the low outlet O_2 concentrations indicate sub-stoichiometric conditions within the cyclone. Char burnout varied from 35 – 65% and gas temperatures were in the range of 1850 – 2150 K. The outlet gas

temperatures are mildly sensitive to the char combustion model, with a difference less than 150 K between the two methodologies.

4.2 Introduction

The partitioning of the incoming ash between the slag layer and fly-ash and the particle size distribution (PSD) of the fly-ash are functions of: the evolving particle size distribution and densities of the combusting particle, velocities within the cyclone, and ash composition. The first three factors impact the aerodynamics of the fuel particle as well as its residence time. Ash composition and particle temperature play a role in the sticking propensity or capture of the particle in the slag layer. Cyclones are often operated in a fuel-rich environment, so some unburnt carbon exiting the cyclone is expected. Over-fire air ports above the cyclone section of the boiler complete the combustion process.

Predicting the simultaneous evolution of the PSD and densities is challenging. There were two modeling approaches employed. The first was a constant diameter approach, where the PSD remains unchanged, and the particle density reduces during the combustion process. The second approach was a constant density model, where the particle density remains unchanged and the particle diameter decreases during the combustion process. Since a systematic analysis of both these methodologies for coal combustion in a cyclone barrel has not been performed, the goals of this chapter were to gain an understanding of the aerodynamics of the particles within the cyclones, particularly when operated at low loads when the air and fuel flow rates feeding the cyclone are reduced. This was done by keeping the parent fuel PSD constant across all scenarios and assuming zero capture of the fly-ash particles. Therefore, any uncertainties regarding particle capture modeling was eliminated.

4.3 Materials and Methods

4.3.1 Shrinking Core and Shrinking Sphere Models

During the coal combustion process, the coal particles shrink and become more porous. However, when modeling in ANSYS Fluent, there are two options for density models. The first is what's known as shrinking core. This is the default option in ANSYS Fluent. The shrinking core model keeps the diameter of the coal particles constant but decreases the density as it burns. The second model is known as shrinking sphere. This model was implemented in ANSYS Fluent as a user defined function (UDF). In the shrinking sphere model, the coal particles become smaller, while retaining their original density. These two models are shown in Figure 4.1.

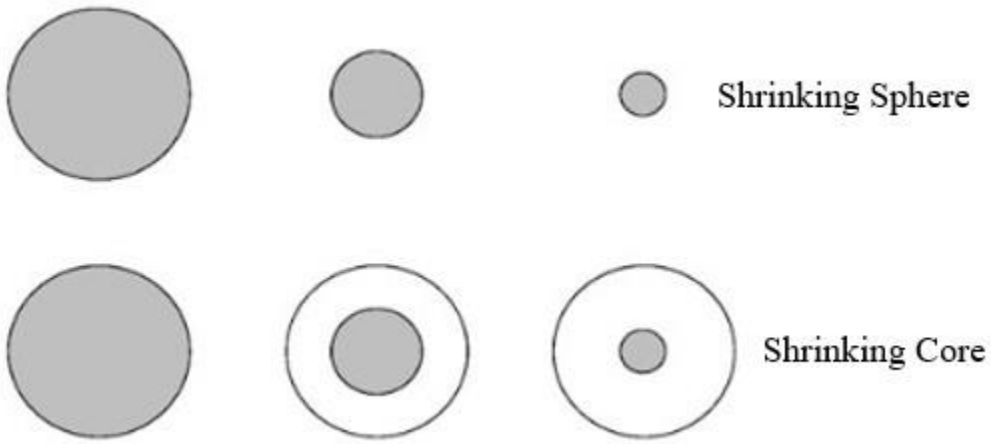

Figure 4.1. Shrinking Core and Shrinking Sphere Char Combustion Models [1]

4.3.2 Cyclone Flow Rates

The geometry of the cyclone barrel and the inlet and outlet ports are shown in Figure 4.2. Pulverized coal is fed in with the primary air. The air and coal inlets are marked by blue arrows and the outlet is marked by red arrows. The cyclone is designed to create a swirling air pattern to reduce slagging at the bottom.

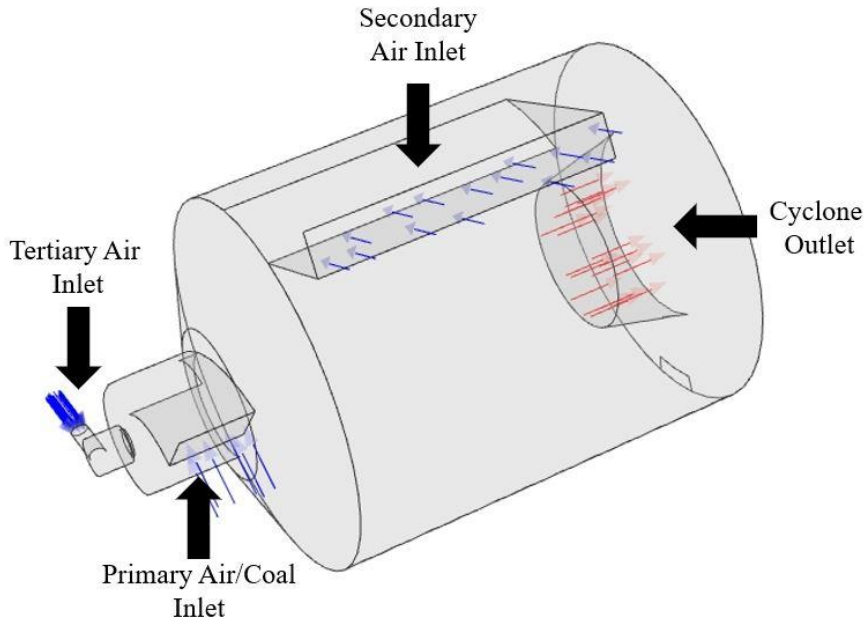

Figure 4.2. Cyclone Inlets and Outlet

The air and coal flow rates corresponding to the different load conditions are summarized in Table 4.1.

Table 4.1 Air and Coal Flow Rates for the Three Loads

Location	50% Load Flow Rate (kg/s)	75% Load Flow Rate (kg/s)	100% Load Flow Rate (kg/s)
Primary Air Inlet	2.9	4.7	4.6
Secondary Air Inlet	15	23	25
Tertiary Air Inlet	0.63	0.63	0.63
Coal Inlet	3.8	5.7	6.6

4.3.3 Selection of Coal Type

Table 4.2 provides the details of the coal ash content. Table 4.3 summarizes the ash composition by weight percent. These values may not sum to 100 due to rounding. Table 4.4 summarizes the proximate and ultimate analysis for the coal used in this study. The formula used for calculating base to acid (B/A) ratio is shown in Equation 4.1.

Table 4.2. Ash Content of the Coal Used for This Study

Case	Silica Content	B/A Ratio	Ash Content
Coal A	High Silica Content (39% by mass)	Low B/A (0.59)	High Ash (10.31%)

The base-to-acid ratio of coal is calculated using the following formula:

$$B/A = \frac{Fe_2O_3+CaO+MgO+K_2O+Na_2O}{SiO_2+Al_2O_3+TiO_2} \quad 4.1$$

Table 4.3 Ash Composition

Compound	Weight Percent
Na_2O	1.5
MgO	1.8
Al_2O_3	15
SiO_2	41
P_2O_5	0.60
SO_3	1.3
Cl	0.30
K_2O	0.50
CaO	28
TiO_2	0.10
Cr_2O_3	0.40
Fe_2O_3	8.6
BaO	1.1

Table 4.4. Coal Proximate and Ultimate Analysis

Coal Case	Coal A
Total Moisture (as rec'd %)	34.47
Ash (as rec'd %)	10.31
Volatile Matter (as rec'd %)	28.75
Fixed Carbon (as rec'd %)	26.47
HHV (as rec'd BTB/lb)	6804
Total Sulfur (as rec'd %)	0.72
Carbon (as rec'd %)	41.24
Hydrogen (as rec'd %)	6.64
Nitrogen (as rec'd %)	0.67
Oxygen by Difference (as rec'd %)	41.24

4.3.4 ANSYS Fluent Inputs and Variables of Interest

Six different cases of the cyclone were run in ANSYS Fluent. These cases were run until they were deemed "converged." Convergence was assessed via an overall energy balance in ANSYS Fluent and by monitoring the gas temperature at the outlet. If the net energy imbalance was less than one percent of the total heat released during the combustion process and the outlet gas temperature was constant, then the case was deemed to be converged.

Results from six simulations are summarized in this chapter based on one coal type, two heterogeneous combustion models, and three operating loads. A summary of combustion models employed in this study are summarized in Table 4.5.

Table 4.5: A Summary of the Combustion Modeling Options Utilized in This Study

Physics being modeled	**Modeling option**
Particle devolatilization (heterogeneous)	Constant rate (50, 1/s) [1, 2]
Char oxidation (heterogeneous)	Shrinking core/shrinking sphere
Volatile combustion (homogeneous) to form products: CO, H_2O, N_2, SO_2	Finite rate/Eddy dissipation [3]
CO oxidation to form CO_2 (homogeneous)	Finite rate/Eddy dissipation [4]
Turbulence	Reynolds Stress Model
Particle Drag law	Morsi-Alexander [5, 6]
Model describing radiative transport	Discrete Ordinates
Particle radiative property	Variable K_{abs} and K_{scat} [Krishnamoorthy and Wolf, 2015]*
Particle scattering phase function	Anisotropic (forward scattering)
Gas-phase radiative property	Perry (5gg) [Krishnamoorthy, 2013]*

*These models were implemented as User-Defined Functions (UDFs) in ANSYS Fluent.

The Reynolds Stress turbulence model was specifically chosen to enable an accurate modeling of the highly anisotropic turbulence characteristics associated with the swirling flow within the cyclone geometry.

The following hypotheses were made:

1. Lower load (50%, 75%) conditions will be associated with longer particle residence times, higher carbon burnout, and higher particle temperatures at the outlet resulting from the lower gas velocities within the cyclone barrel. Therefore, the outlet O_2 mole fractions would be lower also, assuming that the equivalence ratios were identical across the loads.
2. Since the drag experienced by a spherical particle is inversely proportional to the particle Reynolds number, longer residence times associated with the shrinking core methodology are anticipated. This should also translate to higher burnout, higher particle temperatures and lower outlet O_2 mole fractions.

4.4 Results and Discussion

This section will delve into the effect of char combustion models on the outlet cyclone results. All results discussed in this section refer to simulations using Coal A. Table 4.6 shows the mass weighted average residence time of the coal particles exiting the cyclone across the three loads.

Table 4.6. Average Residence Time Across the Three Loads

Load	**Shrinking Core Residence Time (s)**	**Shrinking Sphere Residence Time (s)**
50%	9	17
75%	6	14
100%	10	10

Average particle residence times were in the range of six to seventeen seconds. While the residence time does increase with decreasing loads with the shrinking sphere methodology, there is no identifiable trend for residence time as a function of load for the shrinking core methodology. In addition, residence times with the shrinking sphere model are higher than those of the shrinking core model. Both these predictions are in contrary to the hypothesis stated earlier.

To gain a better understanding of how the coal particles were behaving in the cyclone, particle track figures were created in ANSYS Fluent and are shown in Figure 4.3. For ease of analysis, five to ten representative particles were tracked as they traveled through the cyclone and were colored and sized by two variables: residence time and particle size. Color of the sphere in the tracks represents residence times and the sphere sizes are scaled by particle diameter. Shrinking core particles remain uniform in size, while the shrinking sphere particles slowly shrink as they move down the cyclone. This is to be expected due to the different heterogeneous combustion models. For easier comparison, the range for all six figures was zero to seventeen seconds, due to the highest average residence time of seventeen seconds.

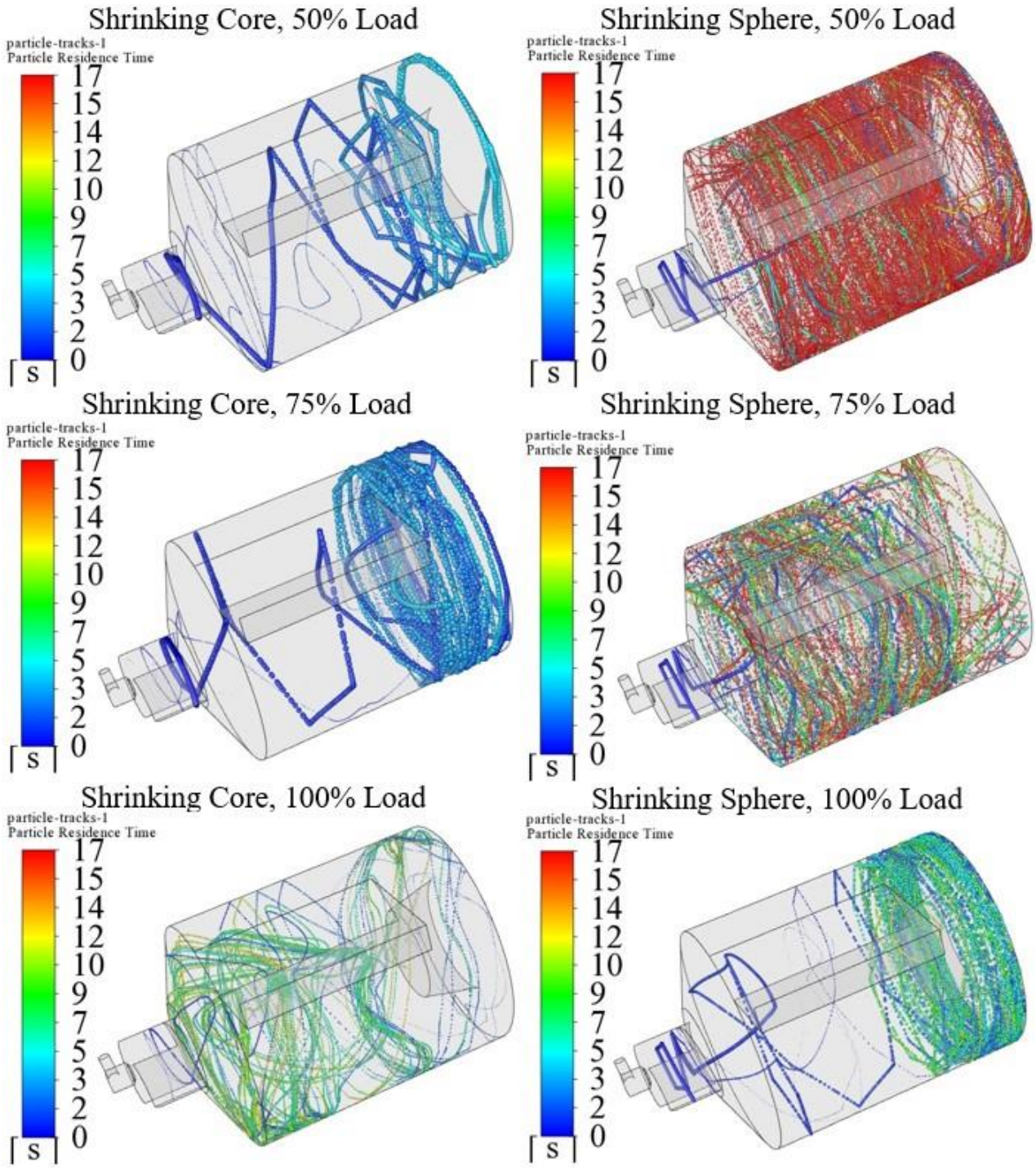

Figure 4.3 (a-f). Particle Tracks for Coal A

The differences in the flow path between the two combustion models gives a better indication of why there is such a stark difference in residence time between the two density

models. First, lower gas velocities cause a more intense circulation of the particles within the cyclone barrel for the shrinking sphere methodology. When looking at these figures, the smaller size particles, such as in the shrinking sphere cases at 50% and 75% loads, have a more swirling and turbulent flow than larger sized particles, such as the shrinking core at 50% load, which results in rebounding of the particles off the walls and a swift exit out of the cyclone.

Figure 4.4 (a-c) compares the effect of the two char combustion models on outlet PSD across the three operating loads. Cumulative mass plots were used to display these distributions, with the average outlet particle diameter for both char combustion models shown in brackets at the bottom of each graph. These were created using a function known as outlet sampling in ANSYS Fluent, where twenty particles at the outlet of the cyclone were analyzed. Using the shrinking core combustion model was associated with a larger average particle size at the outlet and a distribution shifted to the right when compared to the results from the shrinking sphere model. This is due to the fixed diameter of the shrinking core model. The average particle sizes were between 90 and 230 microns larger for the shrinking core methodology than shrinking sphere. The average particle size decreased as the load increased when using the shrinking sphere model. It is important to note that ANSYS Fluent simulations were run using a length scale, so some particles were marked incomplete after swirling for a set length in the cyclone. Swirling particles were generally very fine, so the absence of these particles at the outlet increases the average particle size. The purpose of this portion of the study was to analyze effects of the char combustion model on the outlet PSD, not to obtain highly accurate results for the actual PSD exiting the cyclone.

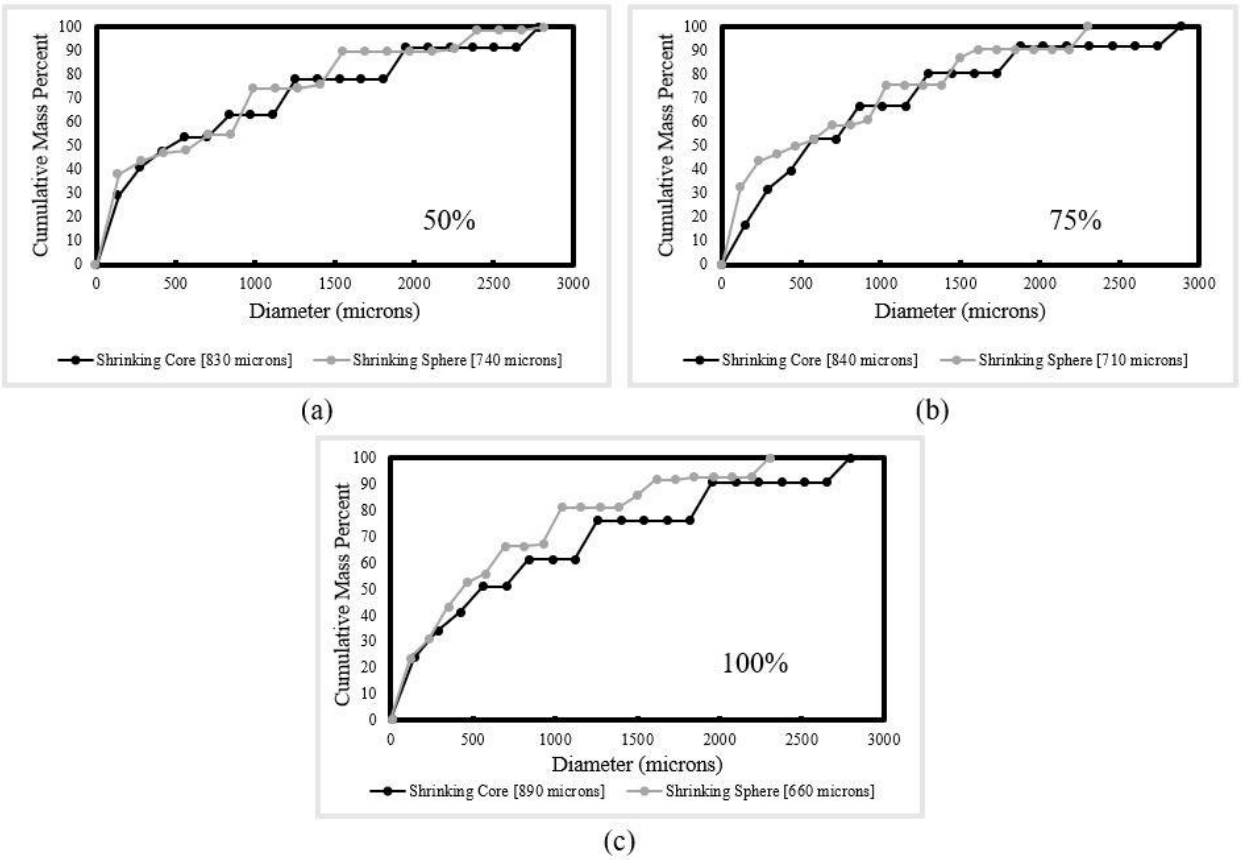

Figures 4.4 (a-c). Outlet PSD for Coal A

Figure 4.5a shows the outlet gas temperature. Gas temperatures were in the range of 1950-2200 K. Outlet gas temperatures were in the range of 1950 to 2200 K. For the shrinking core methodology, the outlet gas temperature increased with load. However, there was no identifiable trend for the shrinking sphere methodology, even when looking at particle residence time. However, the shrinking sphere cases did result in higher outlet temperatures for the 50 and 75% loads, where the residence times were higher.

Figure 4.5b, outlet mole fraction of O_2, is inversely proportional to outlet gas temperatures, indicating more complete combustion. Figure 4.5c represents the percent of carbon burned within the cyclone for all six cases. Due to sub-stoichiometric conditions in the cyclone, there is not 100% conversion of the char at the outlet. Some of these particles will fall to the

bottom of the cyclone, where they will then completely burn, leaving behind a slag layer consisting of ash and minerals. The char burnout is inversely proportional to the outlet oxygen mole fraction for the 75% and 100% loads and is roughly equal for both combustion models at a 50% load.

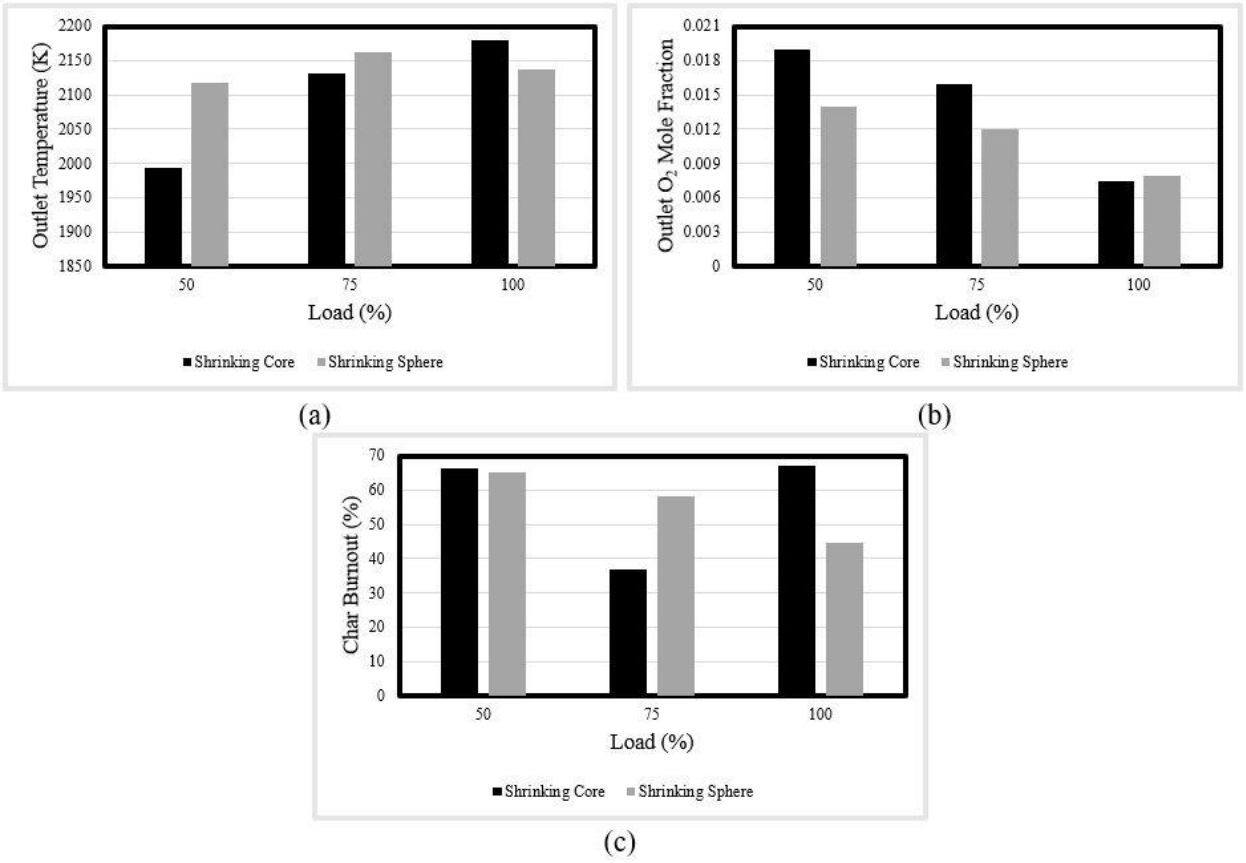

Figure 4.5. (a) Outlet Gas Temperatures; (b) Outlet O_2 Mole Fraction; (c) Char Burnout

4.5 Conclusions

This chapter examined the effects of char combustion model on the combustion characteristics within the cyclone. The residence time in the cyclone varied between five to twenty seconds. The char combustion model and gas velocities have a great impact on the particle tracks. Lower gas velocities, which occur at lower loads, cause the particles to swirl

more towards the back of the cyclone and increase their residence time. Since five to twenty seconds is a sufficiently long residence time to achieve complete combustion for a 100 micron coal particle, the low outlet O_2 concentrations indicate sub-stoichiometric conditions within the cyclone. Char burnout varied from 35 – 65% and gas temperatures were in the range of 1850 – 2150 K. The gas temperatures at the outlet of the cyclone barrel were only mildly sensitive (generally within 150 K) to the char combustion modeling methodology (shrinking core versus shrinking sphere).

References

[1] L. Chen, S.Z. Yong, and A.F. Ghoniem, "Oxy-fuel combustion of pulverized coal: characterization, fundamentals, stabilization and CFD modeling," *Prog. Energy Combust. Sci.*, vol. 38, no. 2, pp. 156-214, Apr. 2012.

[2] M. M. Baum and P. J. Street, "Predicting the combustion behaviour of coal particles," *Combust. Sci. Technol.*, vol. 3, no. 5, pp. 231-243, 1971.

[3] K.W. Ragland and K.M. Bryden, *Combustion Engineering*, 2nd ed. Boca Rotan, FL, USA: CRC Press, 2011.

[4] W.P. Jones and R.P. Lindstedt, "Global reaction schemes for hydrocarbon combustion," *Combust. Flame*, vol. 73, no. 3, pp. 233-249, Sept. 1988.

[5] Ansys, Inc., Canonsburg, PA, USA. *Fluent User's Guide*, Release 2019 R2. (2019). https://ansyshelp.ansys.com/

[6] S.A. Morsi and A.J. Alexander, "An investigation of particle trajectories in two-phase flow

systems," *J. Fluid Mech.*, vol. 55, no. 2, pp. 193-208, Sept. 1972.

Chapter 5 - Sensitivity to Inlet Particle Size Distribution Within the Cyclone

5.1 Abstract

The previous chapters used a good estimate for the inlet particle size distribution entering the cyclones. However, field data collected by MTI allowed us to investigate the operational variabilities in the inlet PSD. From this data, the inlet PSD was altered to fit the mass fractions collected from the power plant. A Rosin-Rammler distribution was used, which is a way to represent a particle size distribution in terms of mass fraction of particles with larger diameters than a selected reference size.

The only alteration made to the initial inlet particle size distribution was changing the mean diameter from 700 microns to 500 microns. This allowed for a Rosin-Rammler curve fit that matched all four samples well. These were the two PSDs used for this study. The goal of this chapter is to analyze the effects that a change in inlet particle size has on the outlet cyclone results, as well as the particle tracks within the cyclone.

Particle residence times were in the range of five to twenty seconds, with the first PSD having higher residence times for the 50% and 75% loads. Outlet gas temperatures were in the range of 1950-2200 K. The second PSD had higher outlet gas temperatures for the 50% and 100% loads. Inlet particle sizes seem to primarily dictate the outlet particle sizes, but have little effect on the outlet gas temperatures or char burnouts. Future studies should use different ranges and spreads for the inlet Rosin-Rammler distribution to gain a better understanding of inlet PSD impacts. However, the second PSD fits the power plant pulverized coal better, so the outlet cyclone results are a better reflection of the actual results experienced at the power plant.

5.2 Introduction

This chapter focuses on the effect that the inlet particle size has on the outlet parameters discussed in Chapter 4. Two particle size distributions were used, with the only difference being the mean particle diameter, as is shown in Table 5.1. A Rosin-Rammler distribution is commonly used for fine particles. It is typically shown graphically for the mass fraction of particles greater than the reference particle diameter on the y-axis, with particle size on the x-axis. This is shown in Figure 5.1.

5.3 Materials and Methods

5.3.1 Rosin-Rammler Distribution

Table 5.1. Two Particle Size Distributions Used

	Particle Size Distribution 1	Particle Size Distribution 2
Minimum Diameter (microns)	1	1
Maximum Diameter (microns)	3,000	3,000
Mean Diameter (microns)	700	500
Spread Parameter	0.75	0.75
Number of Diameters	20	20
Diameter Distribution	Rosin-Rammler-Logarithmic	Rosin-Rammler-Logarithmic

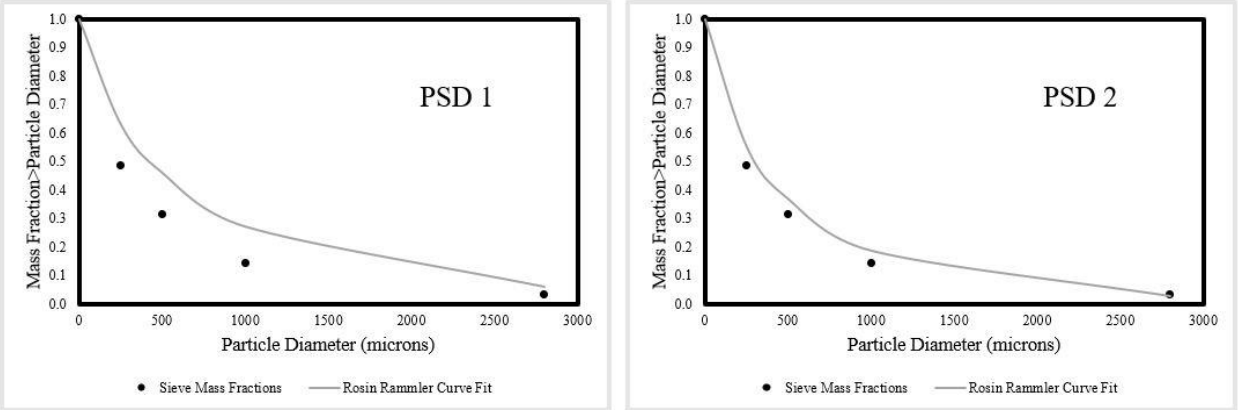

Figure 5.1 (a and b). Particle Size Distribution 1 and 2

These figures were constructed from samples collected at the power station by MTI. Both graphs correlate to Cyclone 3 from the boiler. The Sieve Mass Fractions data set was calculated using mass fractions found from sieving a sample of inlet coal particles entering the third cyclone. The mean diameter was then adjusted to closer fit the mass fractions achieved from the sieves. This is what's known as the Rosin-Rammler Curve, and it is calculated using the following equation [1]:

$$Y_D = \exp\left(-\left(d/\bar{d}\right)^n\right) \tag{5.1}$$

where Y_D is the mass fraction of particles with diameter greater than d. The particle diameter is represented as d, in microns. The sizes used for this study were 250, 500, 1000, and 2800 microns, which correspond to the sieve sizes used. The mean diameter is $\bar{d}$ and the spread parameter is n.

The second particle size distribution has a smaller mean diameter than the first particle size distribution that was used. It was therefore hypothesized that the particle sizes at the outlet would be smaller for PSD 2 than PSD 1. These smaller particles were hypothesized to lead to a lower residence time when compared to PSD 1. Due to the smaller particle sizes, the char burnout should be higher for PSD 2, leading to a higher gas and particle temperature. PSD 2 fits the sieve results from the power plant better. The following results discussed are for coal 1 cases using the shrinking sphere density model.

4.4 Results and Discussion

Table 5.2. Average Residence Time Across the Three Loads

Load	PSD 1 Residence Time (s)	PSD 2 Residence Time (s)
50%	17	13
75%	14	7
100%	10	14

Table 5.2 shows the average particle residence times for the two particle size distributions. Residence times were in the range of seven to seventeen seconds. Particle residence time decreased with increasing load for the second particle size distribution. The second particle size distribution led to a lower residence time for the 50 and 75 percent loads.

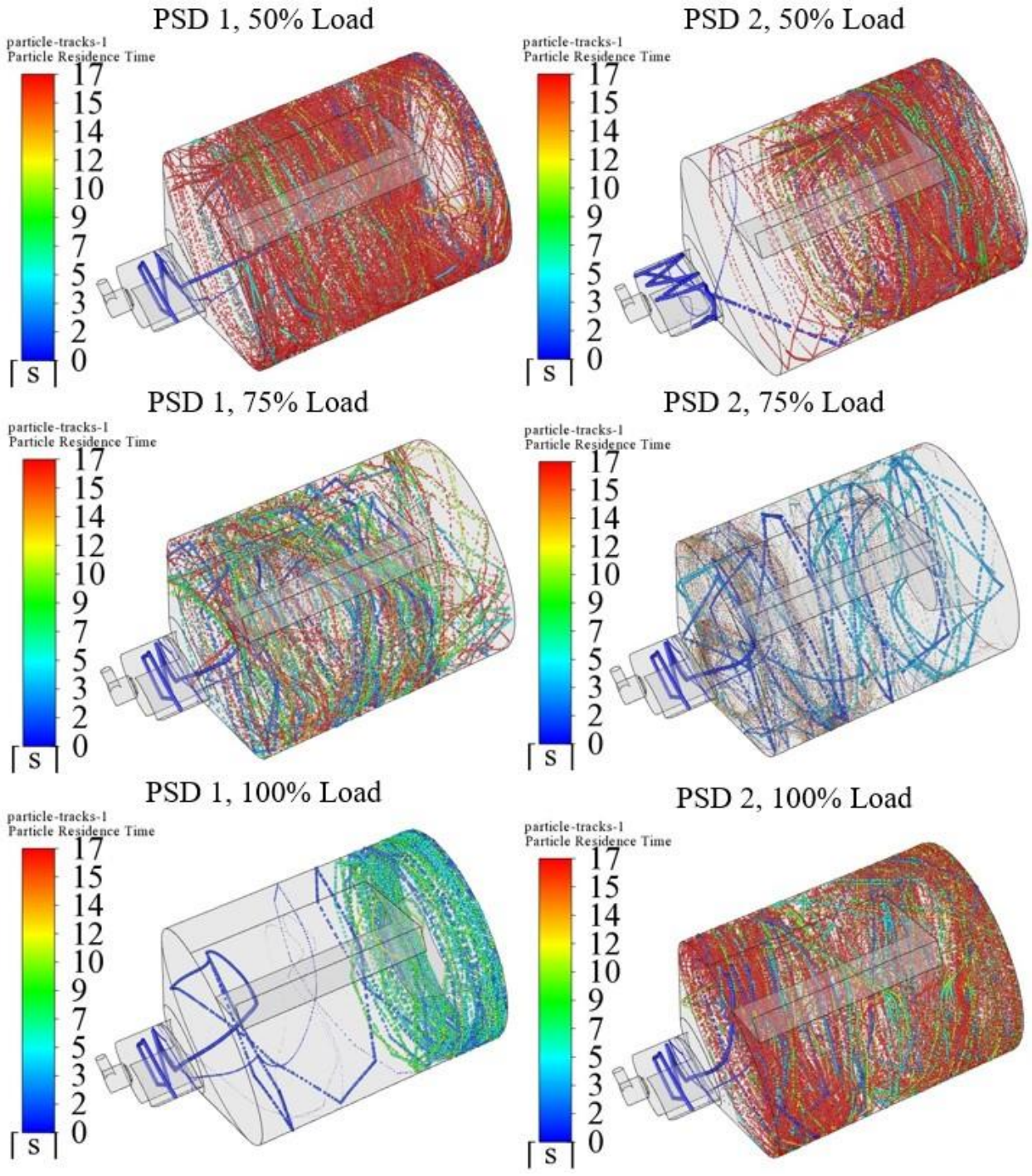

Figure 5.2 (a-f). Particle Tracks for PSD 1 and 2 With Increasing Load

Figure 5.2a-f show the particle tracks comparing the two particle size distributions. These figures show swirling of smaller particles, which is indicative of higher average particle

residence times. Particle tracks agree with the residence times given in Table 5.2, which indicates this is a good representation of the flow pattern occurring within the cyclone.

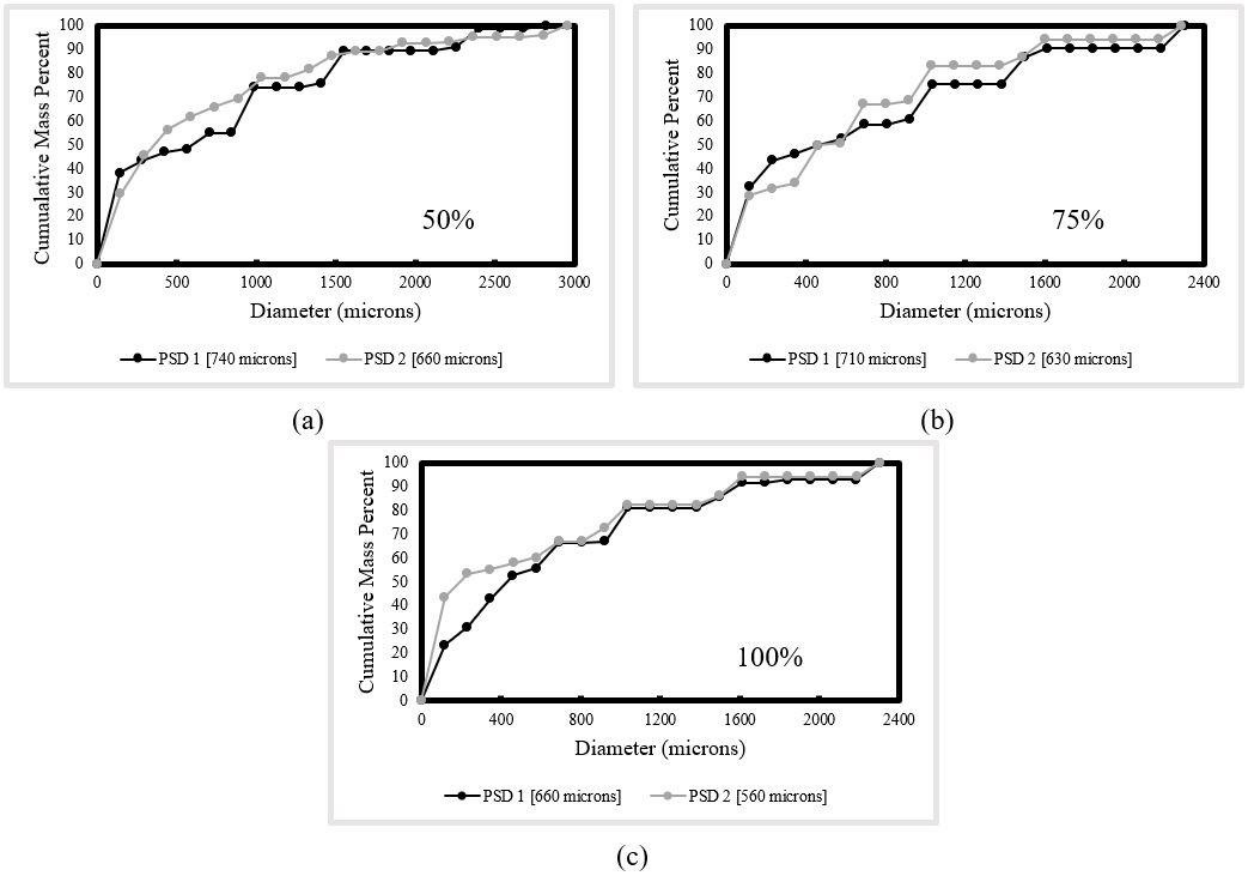

Figure 5.3 (a-c). Outlet PSD for Shrinking Sphere and Coal A for Three Loads

It was expected that PSD 2 would have a lower average particle size at the outlet. This held true for all three loads. Average outlet particle sizes were between 80-100 microns smaller for PSD 2 than PSD 1. Having a smaller inlet mean diameter should lead to a smaller mean diameter at the outlet, which is supported by these PSD outlet figures. The range of particle diameters is roughly the same for both particle size distributions across the three loads. Since the mean inlet diameter was the only aspect of the size distribution that was changed, the range remains the same but the average particle sizes differ.

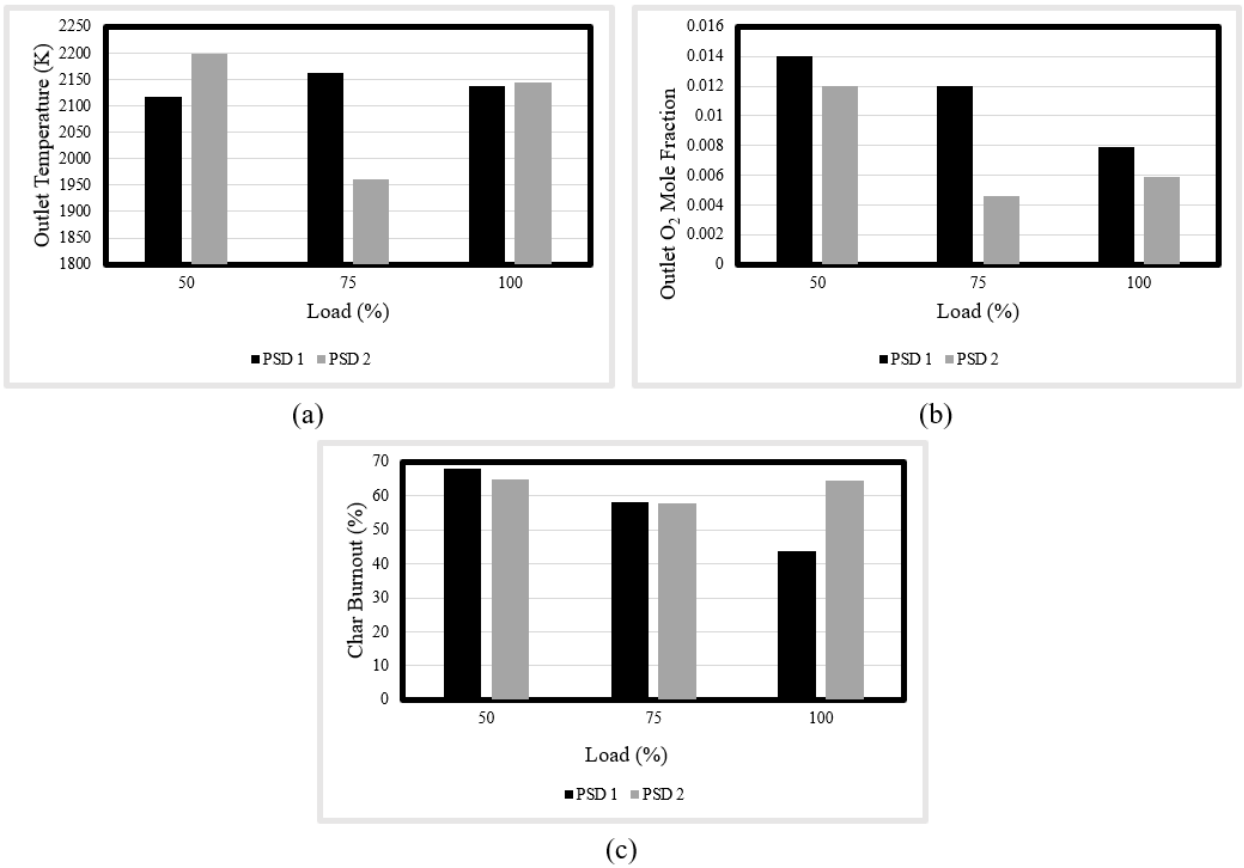

Figure 5.4. (a) Outlet Gas Temperatures; (b) Outlet O_2 Mole Fraction; (c) Char Burnout

Figure 5.4a shows the outlet gas temperatures for the two particle size distributions and three loads. PSD 2 had higher gas temperatures for the 50% and 100% loads, while the 75% load has a temperature which is 200 Kelvin lower, most likely attributed to the relatively low residence time of seven seconds.

It was hypothesized that char burnout should be higher for PSD 2 than PSD 1. This means that the outlet O_2 mole fraction should be lower for PSD 2 than PSD 1. The O_2 mole fraction is lower for PSD 2 across all three loads, but the char burnout is higher for PSD 1 at a 50% load. This could be attributed to the higher residence time for PSD 1 at a 50% load.

The initial hypothesis was that the second size distribution would lead to a higher char burnout. However, this is only the case for the 100% load. The PSD 2 char burnout values are

very close, but slightly less than the PSD 1 values for 50 and 100% loads. Both these loads had a higher residence time for PSD 1, which is the reason for a higher char burnout. The values are very close due to the smaller size of the PSD 2 particles.

5.5 Conclusions

This chapter explored the effects that inlet particle size has on outlet results. Two mean particle sizes were used: 700 and 500 microns. All the simulations used a Rosin-Rammler distribution for the inlet pulverized coal. Residence times were in the range of five to twenty seconds, with the first PSD having higher residence times for the 50% and 75% loads. Outlet gas temperatures were in the range of 1950-2200 K. The second PSD had higher outlet gas temperatures for the 50% and 100% loads. Inlet particle sizes seem to primarily dictate the outlet particle sizes, but have little effect on the outlet gas temperatures or char burnouts. Subsequent studies should use different ranges and spreads for the inlet Rosin-Rammler distribution to gain a better understanding of inlet PSD impacts.

References

[1] Ansys Fluent 12.0 user's guide - 23.3.13 using the rosin-rammler diameter distribution method. (2009, January). https://www.afs.enea.it/project/neptunius/docs/fluent/html/ug/node692.htm

Chapter 6 - Sensitivity to Wall Boundary Conditions Within the Cyclone

6.1 Abstract

Previous simulations for this study used what's known as a "reflect" wall boundary conditions, meaning all particles impacting the cyclone wall will rebound. This chapter will explore the effect of wall boundary conditions within the cyclone. A "trap" boundary condition was also utilized, as well as a particle capture model, which uses a particle kinetic energy and particle viscosity capture criteria.

The trap wall simulations allowed for evaluation of the size of particles impacting the circumferential wall of the cyclone. Large particles (>1200 microns) will be the primary source of particle impaction on the circumferential wall. Very fine particles (<400 microns) are more likely to escape the cyclone without hitting the walls. These particles experience a very low residence time (<1 second) as a result. The "trapping" of large char particles decreases the outlet gas temperatures by roughly 300 K and leads to a smaller range of particle temperatures. This also creates a fuel lean environment in the cyclone, with outlet O_2 mole fractions greater than 0.06 and char burnout in the range of five to fifteen percent. The initial particle capture model, which utilized the critical sticking viscosity and the Urbain viscosity, resulted in no capture of the particles within the cyclone. To account for the highly turbulent and swirling flows that occur in the cyclone, the original particle capture model was refined. This allowed for a slag layer/fly-ash partitioning in the cyclone of roughly 50% for the shrinking sphere cases, which was comparable to previous field test results. Future particle capture studies within cyclone combustion barrels should also use the shrinking sphere methodology for best results.

6.2 Introduction

This chapter focuses on the effect that wall boundary conditions have on the previously discussed results in the previous two chapters. For the purposes of this chapter, only the shrinking sphere model will be used. Previous simulations used all reflect walls, where every particle will rebound off the walls. This chapter uses those simulation results, along with trap wall results, and a particle capture model, which will be described later.

6.3 Materials and Methods

Ash composition has a large impact on the behavior of slag flow and ash deposition in the boiler. Lignite coal varies significantly in the amount of ash and slag forming compounds. There are two types of ash-forming compounds found in the lignite coal. The first type can comprise up to 50% of the ash and is made up of inorganic elements, such as sodium, magnesium, calcium, and potassium, along with the oxygen in the organic phase of the coal. The second type is comprised of mineral grains, such as quartz, clay, and pyrite. These mineral grains are very fine particles that are the source of silicon, aluminum, iron, titanium, and small amounts of calcium and potassium found in this coal. Ranges for ash-forming components in the coal are shown in Table 6.1. These ranges were examined by the project partner MTI from past field tests. The oxides are weight percent of ash expressed as equivalent oxides and the minerals are expressed as weight percent of a mineral basis. Table 6.2 gives the ash composition in weight percent.

Table 6.1. Variability in Ash-Forming Components in Lignite Coal

Component	Range (weight percent)
Na_2O	2.7-16
SiO_2	19-70
CaO	8.9-30
Quartz	0-32
Kaolinite	0.10-11
Montmorillonite	0.20-14

Table 6.2 Ash Composition

Compound	Weight Percent
Na_2O	1.5
MgO	1.8
Al_2O_3	15
SiO_2	41
P_2O_5	0.60
SO_3	1.3
Cl	0.30
K_2O	0.50
CaO	28
TiO_2	0.10
Cr_2O_3	0.40
Fe_2O_3	8.6
BaO	1.1

Another important factor to consider is the inlet flow rate of ash into the boiler. The ash content in the coal used in this boiler varies from 5 to 15% by mass and the moisture content varies from 11 to 36% by mass. Heating values vary from 6400 to 9300 BTU/lb.

Prior field test data has determined that ash content of six to eight percent allows for the best operational conditions for the boiler. A lower ash content than this can cause higher refractory wear on heating tubes. A higher ash content can cause freezing of the slag layer and/or higher ash deposition inside the boiler.

The base-to-acid ratio of coal is calculated using the following formula:

$$B/A = \frac{Fe_2O_3+CaO+MgO+K_2O+Na_2O}{SiO_2+Al_2O_3+TiO_2} \quad 6.1$$

This particular boiler operates best with a base to acid ratio between 0.8 and 1.2. Prior field tests indicate that low and high base to acid ratios can cause oil burning in the cyclones. High base to acid ratios have large amounts of calcium, sodium, and magnesium in the coal. This can lead to crystallization, which results in freezing of the slag layer. Low base to acid ratios

have high levels of aluminum and silicon. This leads to a higher viscosity of the slag layer, impeding its flow out of the cyclone.

Base to acid ratio also plays a role in the deposition of ash in the superheater region of the boiler. A higher base to acid ratio includes more sodium and generally deposits a thin layer on the superheater tubes, with high levels of sticky ash. A lower base to acid ratio generally has a larger quantity of alumino-silicate minerals, which can lead to fast deposit growth. Coal with a higher ash content has a lower base to acid ratio, more silica, and less calcium.

6.3.1 Reflect and Trap Boundary Conditions on the Circumferential Wall

Only the circumferential wall was set to trap, so any particle that impacted that surface was removed from the system. The circumferential wall is shown in Figure 6.1, along with the inlet and outlet arrows for reference.

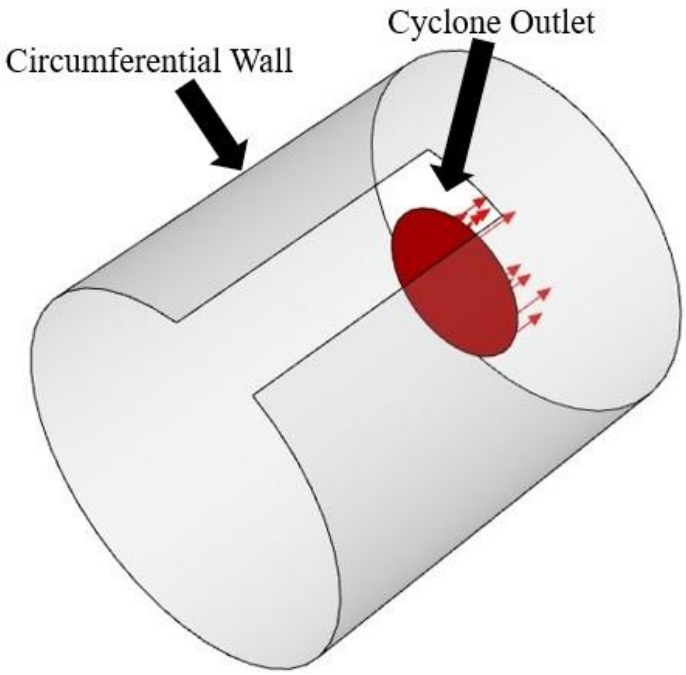

Figure 6.1. Cyclone Circumferential Wall

6.3.2 Particle Capture Model at Circumferential Wall Using Urbain Viscosity Model

Several models with varying degrees of sophistication have been developed over the years to accurately represent the capture phenomena and have been the subject of recent reviews [1]. There are two primary frameworks for modeling particle capture. The first is a molten fraction-based approach, where equilibrium calculations are performed to estimate the molten fraction and used in conjunction with a critical velocity [2]. In this study, a critical particle viscosity-based capture criterion was adopted, where the capture probability (P_{stick}) equals one if the particle viscosity (μ_p) is lower than the critical sticking viscosity ($\mu_{p,critical}$).

$$P_{stick} = 1 \text{ if } \mu_p \leq \mu_{p,critical} \tag{6.2}$$

P_{stick} is zero otherwise. Based on three datasets using similar particle sizes, particle kinetic energy (PKE), and gas velocities associated with this study, the following relationship between PKE and critical viscosity ($\mu_{p,critical}$) proposed by Kleinhans et al. (2018b) was adopted:

$$\mu_{p,critical} = \frac{5\times10^{-12}}{PKE^{1.78}} \tag{6.3}$$

This criterion has been validated for two previous studies. One of which is for ash deposition following combustion of a biomass and coal blend, while the other is ash deposition following pulverized coal. [3, 4] A PKE and particle viscosity criterion has been formulated based on measurements in low velocity (<20 m/s) for non-swirling flows. The goal of this chapter is to extend and refine this capture model to swirling, highly turbulent flows which are present in the cyclone barrel. Critical sticking viscosity is the point at which the slag changes from that of a Newtonian fluid to a plastic fluid upon cooling [5].

In Figure 6.2, the sticking criterion (Equations 6.2 and 6.3) are represented as a function of particle viscosity (μ_p) and particle kinetic energy (PKE) is represented as a diagonal line defining the sticking and rebounding conditions.

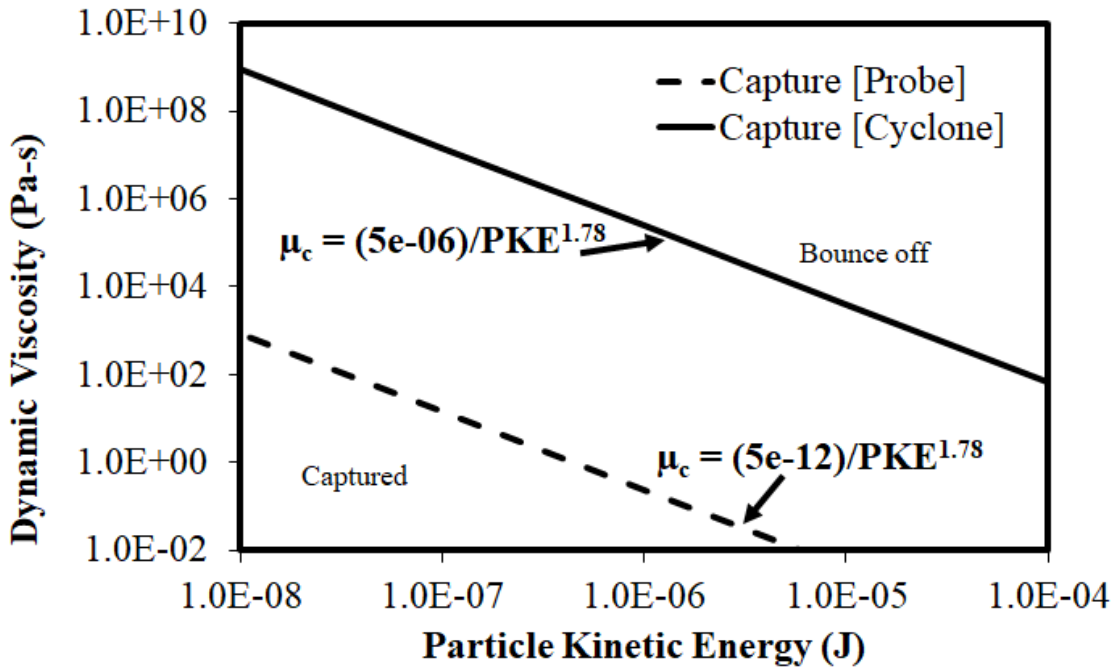

Figure 6.2. Particle Sticking Criterion as a Function of Particle Viscosity and Particle Kinetic Energy [1, 5]

This particle capture criteria is dominated by inertial impaction, which is considered as the most important mechanism that contributes significantly to the ash deposition build-up process. This process takes place when these particles, primarily with diameters greater than 10 microns, have adequate inertia to follow the gas flow and collide on the heat exchange surface by inertial forces [5].

In the high temperature region within the cyclone, the Urbain viscosity model parameters were employed to model the compositional and temperature dependencies of the particle

viscosity. Urbain assumes that slag is positional changes of the ionic structure into free spaces depending on the free volume probability, P_v. The next assumption is that viscosity is a function of the "jumping" probability, P_e, of the slag. Urbain also separates the model into three ions, network forming, network modifying, and amphoteric ions [6]. These ions are shown in Table 6.3.

Table 6.3. Urbain Model Ion Groups [6]

Classification	Ion
Network Former	Si^{4+}, Ge^{4+}, P^{5+}
Network Modifier	Na^{+}, K^{+}, Ca^{2+}, Fe^{2+}, Cr^{3+}, Ti^{4+}
Amphoteric	Al^{3+}, B^{3+}, Fe^{3+}

The Urbain viscosity model uses parameters A and B, which depend only on the melt composition of the coal. Constant α is used to describe the fraction of network modifiers and amphoterics. MO is the mole fraction of network modifiers and A_2O_3 is the mole fraction of amphoterics. The following equations give the Urbain viscosity for the slag as a function of temperature:

$$\mu_p = A \times T \times \exp\left(\frac{1000B}{T}\right) \tag{6.3}$$

Where μ_p is the Urbain particle viscosity, T is particle temperature in Kelvin, A and B are empirical parameters, which are defined using the following set of equations:

$$A = exp(0.2693B - 13.9751) \ \left[\frac{Pa\ s}{K}\right] \tag{6.4}$$

$$B = B_0 + B_1 \times N + B_2 \times N^2 + B_3 \times N^3 \tag{6.5}$$

$$N = molar\ fraction\ of\ silica$$

$$B_0 = 13.8 + 39.9355 \times \alpha - 44.049 \times \alpha^2 \tag{6.6}$$

$$B_1 = 30.481 - 117.1505 \times \alpha + 129.9978 \times \alpha^2 \quad 6.7$$

$$B_2 = -40.9429 + 234.0486 \times \alpha - 300.04 \times \alpha^2 \quad 6.8$$

$$B_3 = 60.7619 - 153.9276 \times \alpha + 211.1616 \times \alpha^2 \quad 6.9$$

$$\alpha = \frac{\sum MO}{\sum MO + \sum A_2O_3} \quad 6.10$$

$$MO = CaO + MgO + FeO + MnO + TiO_2 + Na_2O + K_2O \quad 6.11$$

$$A_2O_3 = Al_2O_3 + Fe_2O_3 \quad 6.12$$

The temperature dependence of the Urbain viscosity is shown in Figure 6.3.

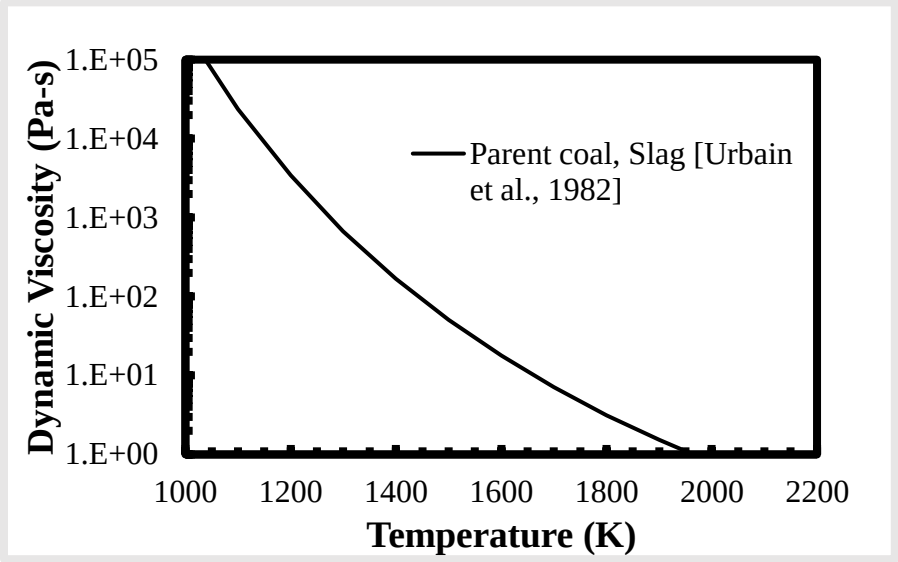

Figure 6.3. Temperature Dependence of Urbain Viscosity Model [7]

6.4 Results and Discussion

Table 6.4. Average Residence Time Across the Three Loads

Load	Reflecting Walls Residence Time (s)	Trap Wall Residence Time (s)
50%	17	0.22
75%	14	0.44
100%	10	0.25

Table 6.4 shows the average particle residence time between reflect and trap walls for the three loads. The trap walls all have average residence times between 0.2-0.45 s. This indicates that the larger particles are the ones hitting the circumferential wall and being removed. This means that the residence times for the trap wall are very small particles that are entrained in the gas stream and quickly exit the cyclone. Larger particles that bounce off the circumferential wall for the reflect boundary condition bring up the average residence time significantly.

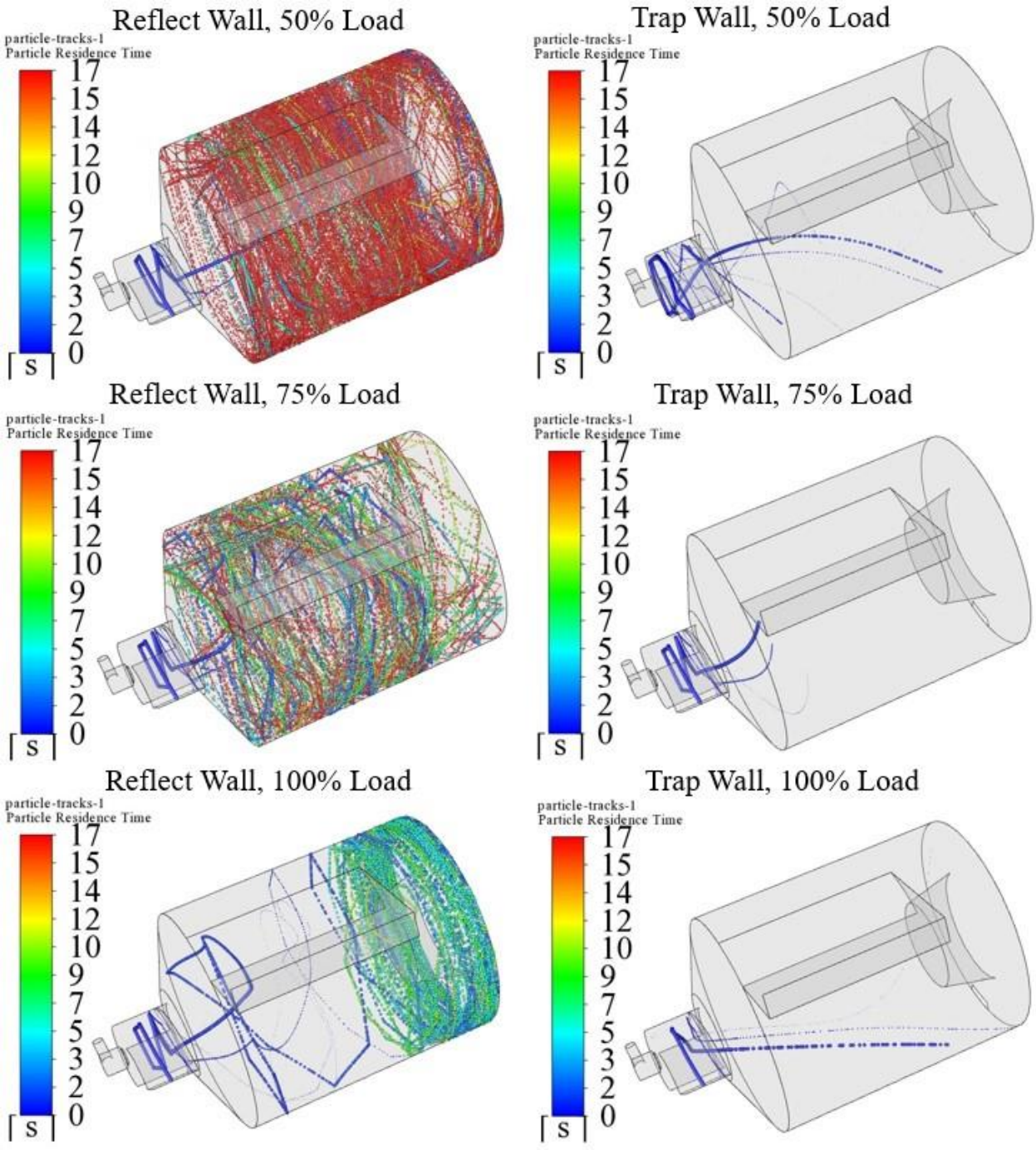

Figure 6.4 (a-f). Particle Tracks for Reflect and Trap Wall for Three Loads

Figure 6.4 (a-f) show the particle tracks for reflect and trap boundary conditions across the three loads. The figures on the left (reflect boundary conditions) all show larger particles bouncing off the walls. However, the figures on the right (trap boundary conditions) show large

particles hitting the wall and being removed from the system. The only particles that can be seen traveling close to the cyclone outlet are very fine particles. This also supports the residence time table discussed previously. The larger particles are being removed, which drastically decreases the average residence time.

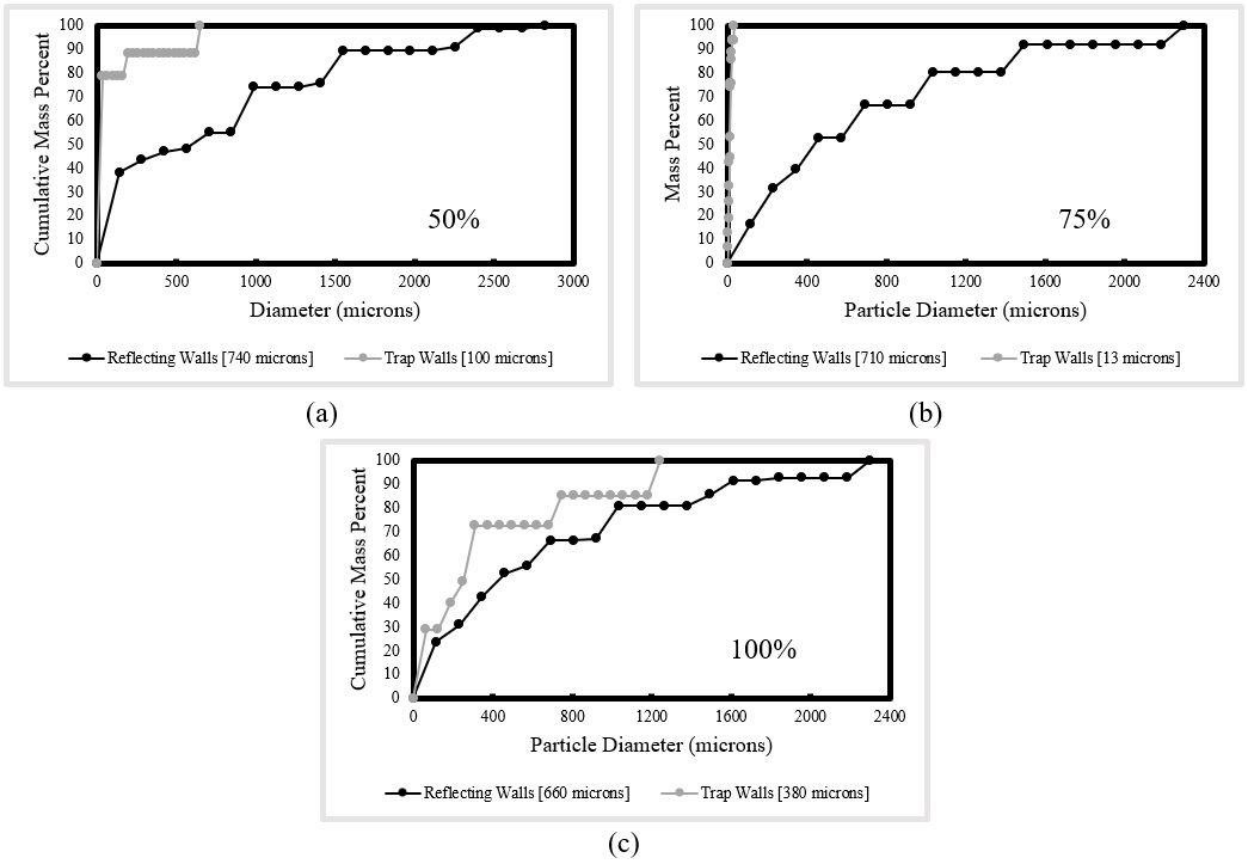

Figure 6.5 (a-c). Outlet PSD for Reflect and Trap Wall Across All Loads

Figure 6.5 shows the outlet particle size distribution for reflect and trap boundary conditions across the three loads. The trap wall leads to an average particle diameter between 13 to 380 microns. The largest sampled outlet particle recorded for any of the trap simulations was around 1200 microns in diameter, while the largest for any of the reflect simulations was around 2800 microns. This indicates that particles larger than this will not be subject to the flow of the gas, leading to possible impaction with the circumferential wall.

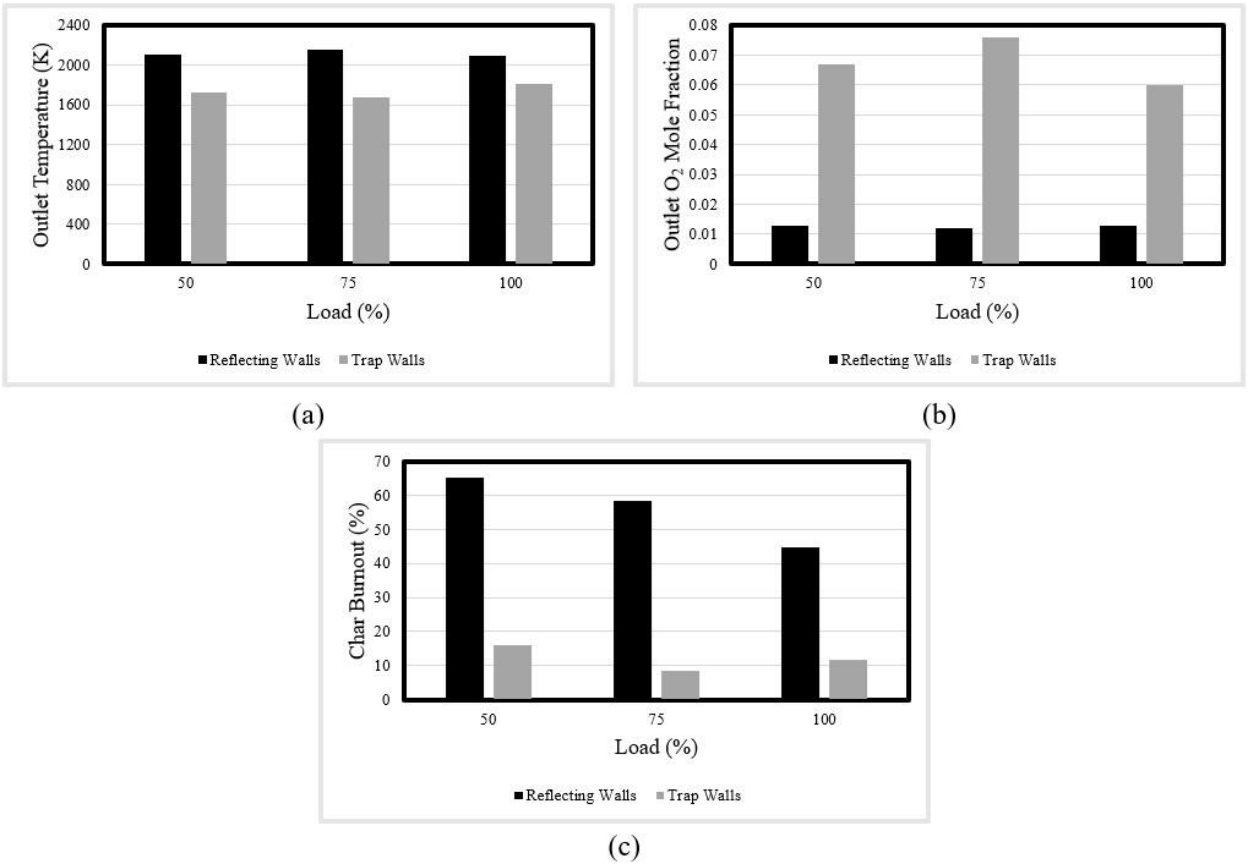

Figure 6.6. (a) Outlet Gas Temperatures; (b) Outlet O_2 Mole Fraction; (c) Char Burnout

Switching to a trap circumferential wall led to an average decrease in outlet gas temperature of 390 K. This is due to the removal of coal particles from the system, as well as the very low residence time of the remaining particles. The outlet O_2 mole fraction shoots up to 0.06-0.08 when the circumferential wall is set to trap. This is above the 0.03 threshold that is desired for the cyclone. The removal of particles from the cyclone creates a fuel lean environment within the cyclone. Char burnout decreases to five to fifteen percent for the trap wall simulations as a result of large particles being removed and a very low residence time of exiting particles.

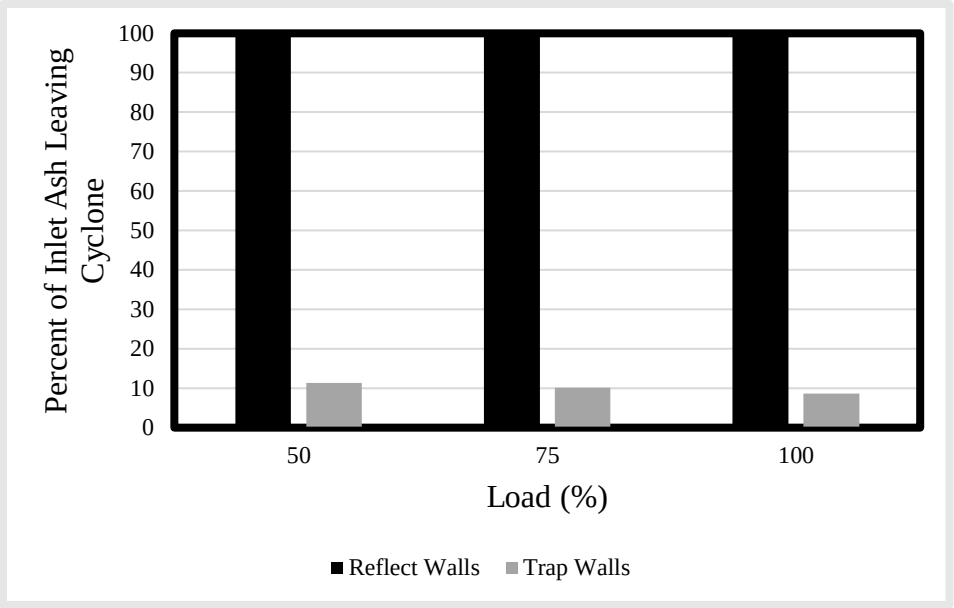

Figure 6.7. Fly Ash Percent for Reflect vs Trap Walls

Figure 6.7 shows the comparison of fly ash percent for reflect and trap boundary conditions. This graph assumes the particles for the reflect wall boundary condition are allowed to bounce around the cyclone walls endlessly until they eventually exit the cyclone. Switching the circumferential wall to a trap boundary led to an average drop of 90 percent for each load in the amount of fly ash leaving the cyclone. This is due to the removal of large particles that would otherwise rebound if a reflect boundary was used. Figure 6.7 shows the extremes for the partitioning of fly-ash leaving the cyclone. The actual partitioning should be somewhere between these two extremes.

Table 6.5 shows the results from the inertial impaction particle capture model in the cyclone for both coal cases, density models, and three loads. Applying the particle capture model led to very little mass captured by the wall, if any particles at all. This indicates that the particle kinetic energy-based particle capture model implemented after the secondary superheater is not adequate within the cyclone, most likely because of the highly turbulent, swirling flows.

Table 6.5. Particle Capture Model Results

Case	Percent of Total Ash Captured in Slag Layer
Shrinking Core, 50%	8.5e-04
Shrinking Core, 75%	0
Shrinking Core, 100%	1.8e-04
Shrinking Sphere, 50%	3.1e-04
Shrinking Sphere, 75%	0
Shrinking Sphere, 100%	3.5e-04

Due to the highly turbulent, swirling flows within the cyclone, a more stringent criteria for particle capture was required. The underlying assumption was that the force of impaction of a particle impacting the cyclone wall via angular momentum would be far less than the same particle traveling at the same speed and hitting a cylindrical probe straight on. The critical viscosity was adjusted from $\frac{5\times10^{-12}}{PKE^{1.78}}$ to $\frac{5\times10^{-6}}{PKE^{1.78}}$ to account for the swirling flow experienced in the cyclone. The sticking and rebounding criteria for the probe and cyclone deposition simulations is shown in Figure 6.8. The results from this new particle capture model are shown in Table 6.6. Mass fractions in this table may not sum to one hundred due to rounding. This was done for both shrinking core and shrinking sphere. The second particle size distribution was used because that matched the pulverized coal samples better than the original particle size distribution.

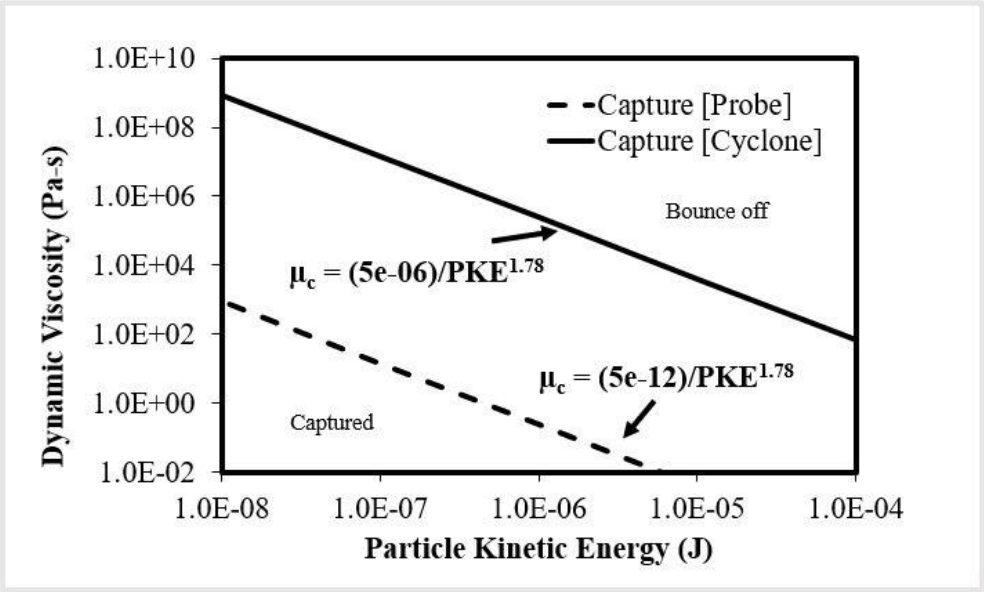

Figure 6.8. Modified Particle Capture Model for the Cyclone

Table 6.6. Modified Particle Capture Results for Shrinking Core Char Combustion Model

Cyclone Load	Percent of Total Ash Captured in Slag Layer	Percent of Captured Particles with PKE < 1e-06 J	Percent of Captured Particles with 1e-06 J < PKE < 1e-4 J	Percent of Captured Particles with PKE > 1e-04 J
Shrinking Core, 50%	46	16	53	31
Shrinking Core, 75%	11	8	46	46
Shrinking Core, 100%	39	23	4	72
Shrinking Sphere, 50%	52	21	55	24
Shrinking Sphere, 75%	46	19	49	32
Shrinking Sphere, 100%	50	17	48	35

The shrinking sphere methodology results agree with the expected partitioning in the cyclone much better than the initial model results shown in Table 6.4. The correction factor placed on the capture criteria allowed for adequate representation of the sticking probabilities in the cyclone.

6.5 Conclusions

This chapter explored the effects of wall boundary conditions within the cyclone. Reflect and trap walls were used, along with a particle kinetic energy-based capture model. The trap wall simulations allowed for evaluation of the size of particles impacting the circumferential wall of the cyclone. Large particles (>1200 microns) will be the primary source of particle impaction on the circumferential wall. Very fine particles (<400 microns) are more likely to escape the cyclone without hitting the walls. These particles experience a very low residence time (<1 second) as a result. The removal of large char particles decreases the outlet gas temperatures by roughly 300 K and leads to a smaller range of particle temperatures. The initial particle capture model, which utilized the critical sticking viscosity and the Urbain viscosity, resulted in no capture of the particles within the cyclone. To match ash partitioning results given by MTI, a correction factor of one million was multiplied to the critical viscosity. This allowed for a slag layer/fly-ash partitioning of roughly 50% within the cyclone for the shrinking sphere cases, which was comparable to previous field test results. This indicates that inertial impaction for highly turbulent and swirling flows needs to be adjusted for an adequate representation of particle capture using a model which is typically designated for fairly linear flow.

References

[1] Kleinhans, U., Wieland, C., Frandsen, F.J., Spliethoff, H., 2018b. Ash formation and deposition in coal and biomass fired combustion systems: progress and challenges in the field of ash particle sticking and rebound behavior. Progr Energy Combust 68:65-168

[2] Cai, Y., Tay, K., Zheng, Z., Yang, W., Wang, H., Zeng, G., Li, Z., Keng Boon, S., &

Subbaiah, P. (2018). Modeling of ash formation and deposition processes in coal and biomass fired boilers: A comprehensive review. *Applied Energy*, *230*, 1447–1544. https://doi.org/10.1016/j.apenergy.2018.08.084

[3] Gautham Krishnamoorthy, "Modeling ash deposition and shedding during oxy-combustion of coal/rice husk blends at 70% inlet O2," International Journal of Coal Science & Technology (2023) 10:27, https://doi.org/10.1007/s40789-023-00583-8

[4] Gautham Krishnamoorthy, "Aerodynamic Influences on the Outer Ash Deposition Rates during Oxy-Coal Combustion." Cleaner Chemical Engineering (2022), https://doi.org/10.1016/j.clce.2022.100057.

[5] Ye, Insoo, et al. "Influence of Critical Viscosity and Its Temperature on the Slag Behavior on the Wall of an Entrained Coal Gasifier." *Applied Thermal Engineering*, vol. 87, 2015, pp. 175–184.,

[6] A. Bronsch, "Viscosity of Slags," Ph.D. dissertation, Department of Mechanical, Process, and Energy Engineering, Technical University Bergakademie Freiberg, 2017.

[7] Urbain, G. (1987). Viscosity estimation of Slags. *Steel Research*, *58*(3), 111–116. https://doi.org/10.1002/srin.198701513

Chapter 7 - Conclusions and Recommendations for Future Work

7.1 Conclusions

Chapter three focused heavily on gas temperatures and velocities within the full boiler. At higher loads, the gas temperatures exceed 2000 K near the over-fired air ports. There were four primary areas of interest for analyzing gas temperatures in the boiler: the nose gas plane, secondary superheater inlet, secondary superheater outlet, and the reheater outlet. ANSYS Fluent gas temperatures were in the range of 1000-1500 K for the nose gas plane, 900-1400 K for the secondary superheater inlet, 850-1250 K for the secondary superheater outlet, and 800-1000 K for the reheater outlet. These results are a good representation of the gas temperatures given by the power plant. Gas temperatures decrease with lower loads. There was no identifiable trend for temperature maldistributions with a decrease in load.

The velocity profile was more uniform at higher loads, with higher velocity magnitudes as well. There was no trend for velocity maldistributions as the load fluctuated. The reheater outlet had a coefficient of variation that was roughly double the nose gas and secondary superheater inlet/outlet. This is a result of the turn of gas flow caused by the geometry of the reheater and boiler.

The particle kinetic energy-based capture criteria was able to adequately represent deposition rates given by MTI after the secondary superheater. The numerical results were higher than the rates that were experimentally measured. This is due to the clean surface assumption for all the particles impacting the probe during the numerical simulations, where the experimental measurements didn’t have a clean probe surface after the initial layer was deposited.

Chapter four examined the effects of char combustion model on the combustion characteristics within the cyclone. The residence time in the cyclone varied between five to twenty seconds. The char combustion model and gas velocities have a great impact on the particle tracks, but not on outlet gas temperatures, which were at most a 150 K difference between the two combustion models. Lower gas velocities, which occur at lower loads, cause the particles to swirl more towards the back of the cyclone and increase their residence time. Five to twenty seconds is a sufficiently long residence time to achieve complete combustion for a 100 micron diameter coal particle. Therefore, the low outlet O_2 concentrations indicate sub-stoichiometric conditions within the cyclone. Char burnout varied from 35 – 65% and gas temperatures were in the range of 1850 – 2150 K.

Chapter five analyzed the effects that inlet particle size has on outlet results. Two mean particle sizes were used: 700 and 500 microns. All the simulations used a Rosin-Rammler distribution for the inlet pulverized coal. Residence times were in the range of five to twenty seconds, with the first PSD having higher residence times for the 50% and 75% loads. Outlet gas temperatures were in the range of 1950-2200 K. The second PSD simulations resulted in higher outlet gas temperatures for the 50% and 100% loads. Inlet particle sizes seem to primarily dictate the outlet particle sizes, but have little effect on the outlet gas temperatures or char burnouts. Subsequent studies should use different ranges and spreads for the inlet Rosin-Rammler distribution to gain a better understanding of inlet PSD impacts. Future studies should use the second PSD because it matched the pulverized inlet coal field measurements.

Chapter six explored the effects of wall boundary conditions within the cyclone. Reflect and trap walls were used, along with a particle kinetic energy-based capture model. The trap wall simulations allowed for evaluation of the size of particles impacting the circumferential wall of

the cyclone. Most large particles (>1200 microns) will impact the circumferential wall. Very fine particles (<400 microns) are more likely to escape the cyclone without hitting the walls. These particles experience a very low residence time (<1 second) as a result, indicating the large particles are the ones that drive the average residence time up. The removal of large char particles decreases the outlet gas temperatures by roughly 300 K and leads to a smaller range of particle temperatures. The initial particle capture model, which utilized the critical sticking viscosity and the Urbain viscosity, resulted in no capture of the particles within the cyclone. To match ash partitioning results given by MTI, a correction factor of one million was multiplied to the critical viscosity. This was done to account for the swirling flow experienced within the cyclone. This allowed for a slag/fly-ash partitioning of roughly 50% within the cyclone for the shrinking sphere cases, which was comparable to results given by MTI.

7.2 Future Work

Many indices and mechanistic models have been developed in the literature to predict deposition, but they are specific for certain boilers and fuels and cannot be generalized. In addition to that, they are not able to predict the most critical areas where fouling and slagging occur and the effect of deposit accumulation on heat transfer. For such a complex subject, CFD has been recognized as one of the best tools to study deposition onto heat exchangers as it allows calculation of both gas and particle behavior, including deposition flux and modeling mass and heat transfer [1]. Further studies can use current converged cases to model different ash deposition mechanisms, such as thermophoresis and condensation reactions.

Using the particle capture model for the full boiler and cyclone simulations would give a better understanding of the outlet cyclone PSD, as well as ash deposition behavior in the entire convective pass. This could allow for different deposition mechanisms to explore, such as

thermophoresis and condensation. Future studies should explore the growth of deposits after the initial layer is formed. Future studies in the heat extraction rate in the convective pass, as well as radiative heat transfer would also be useful in ensuring accuracy of flue gas temperatures at all regions in the boiler. This could also be used as a guide for boiler efficiency as a function of load. Another future opportunity would be continuing this work with slagging in entrained flow gasifiers.

When operating in low loads, the power plant will turn on and off select cyclones. It would be useful to simulate the full boiler under varied operational cyclones to identify any possible combination that would create the most uniform temperature and velocity profiles. Varying the inlet cyclone PSD by adjusting the spread parameter and the range of particle sizes. Changing the mean inlet particle size had little effect on outlet temperatures, so it would be interesting to gain a better understanding on how great an impact particle size distribution has on the combustion characteristics within the cyclone. Lastly, it would be very helpful to develop a model that accurately predicts the evolving density and diameter of coal particles during the combustion process. This would be useful in ensuring accuracy in the fly-ash PSD and the ash partitioning within the cyclone, which would improve numerical predictions of ash deposition in the superheater region of the boiler.

References

[1] Riccio, C., Simms, N. J., & Oakey, J. E. (2019). Deposition prediction in a pilot scale pulverized fuel-fired combustor. *Fuel*, *253*, 1204–1213. https://doi.org/10.1016/j.fuel.2019.05.077